

The Radiation Assessment Detector (RAD) Investigation

D.M. Hassler · C. Zeitlin · R.F. Wimmer-Schweingruber · S. Böttcher · C. Martin · J. Andrews · E. Böhm · D.E. Brinza · M.A. Bullock · S. Burmeister · B. Ehresmann · M. Epperly · D. Grinspoon · J. Köhler · O. Kortmann · K. Neal · J. Peterson · A. Posner · S. Rafkin · L. Seimetz · K.D. Smith · Y. Tyler · G. Weigle · G. Reitz · F.A. Cucinotta

Received: 11 January 2012 / Accepted: 15 June 2012
© Springer Science+Business Media B.V. 2012

Abstract The Radiation Assessment Detector (RAD) on the Mars Science Laboratory (MSL) is an energetic particle detector designed to measure a broad spectrum of energetic particle radiation. It will make the first-ever direct radiation measurements on the surface of Mars, detecting galactic cosmic rays, solar energetic particles, secondary neutrons, and other secondary particles created both in the atmosphere and in the Martian regolith. The radiation environment on Mars, both past and present, may have implications for habitability and

D.M. Hassler (✉) · C. Zeitlin · J. Andrews · M.A. Bullock · B. Ehresmann · K. Neal · J. Peterson · S. Rafkin
Southwest Research Institute, Boulder, CO, USA
e-mail: hassler@boulder.swri.edu

R.F. Wimmer-Schweingruber · S. Böttcher · C. Martin · E. Böhm · S. Burmeister · J. Köhler · O. Kortmann · L. Seimetz
Christian Albrechts University, Kiel, Germany

D.E. Brinza
NASA Jet Propulsion Laboratory, Pasadena, CA, USA

M. Epperly · K.D. Smith · Y. Tyler · G. Weigle
Southwest Research Institute, San Antonio, TX, USA

D. Grinspoon
Denver Museum of Nature and Science, Denver, CO, USA

O. Kortmann
Space Sciences Laboratory, Berkeley, CA, USA

A. Posner
NASA Headquarters, Washington, DC, USA

G. Reitz
Deutsches Zentrum für Luft- und Raumfahrt, Köln, Germany

F.A. Cucinotta
NASA Johnson Space Center, Houston, TX, USA

the ability to sustain life. Radiation exposure is also a major concern for future human missions. The RAD instrument combines charged- and neutral-particle detection capability over a wide dynamic range in a compact, low-mass, low-power instrument. These capabilities are required in order to measure all the important components of the radiation environment.

RAD consists of the RAD Sensor Head (RSH) and the RAD Electronics Box (REB) integrated together in a small, compact volume. The RSH contains a solid-state detector telescope with three silicon PIN diodes for charged particle detection, a thallium doped Cesium Iodide scintillator, plastic scintillators for neutron detection and anti-coincidence shielding, and the front-end electronics. The REB contains three circuit boards, one with a novel mixed-signal ASIC for processing analog signals and an associated control FPGA, another with a second FPGA to communicate with the rover and perform onboard analysis of science data, and a third board with power supplies and power cycling or “sleep”-control electronics. The latter enables autonomous operation, independent of commands from the rover. RAD is a highly capable and highly configurable instrument that paves the way for future compact energetic particle detectors in space.

Keywords MSL · Mars Science Laboratory · Mars · Mars radiation environment · Radiation · Human exploration detectors in space

1 Introduction

The Radiation Assessment Detector (RAD) investigation is an investigation to detect and analyze the most biologically hazardous energetic particle radiation on the Martian surface as part of the Mars Science Laboratory (MSL) mission. There are two primary types of energetic particle radiation incident at the top of the Mars atmosphere, Galactic Cosmic Rays (GCRs) and Solar Energetic Particles (SEPs). Both GCRs and SEPs interact with the atmosphere and penetrate into the soil where they produce secondary particles—including neutrons and γ -rays—that contribute to the radiation environment on the surface. This radiation environment, and the associated health risks to astronauts, will have a major impact on the planning of any future human missions to Mars (Cucinotta et al. 2001). The surface radiation environment also affects any potential organisms, presumably dormant, that may have survived underground (Pavlov et al. 2002; Dartnell et al. 2007a; Cucinotta et al. 2007); and surface radiation measurements by RAD may give insight into the chemical alteration of the regolith caused by space radiation on long time scales (Schwadron et al. 2012).

The RAD instrument has a wide dynamic range for charged particles and is able to measure all ion species that contribute to the radiation exposure on the surface of Mars (Fig. 1) with a geometry factor of $\sim 0.9 \text{ cm}^2 \text{ sr}$ (see Sect. 3.1.1 for details). Similar to other compact particle telescopes (e.g. SOHO/COSTEP-EPHIN, Müller-Mellin et al. 1995), RAD provides differential fluxes in limited energy ranges, about 10–100 MeV/nuc for protons and helium, and integral fluxes of ions with higher energies. The dE/dx resolution of RAD is sufficient to distinguish between major particle species. RAD measures dE/dx in silicon, but these measurements can also be related to Linear Energy Transfer (LET) in water. (By LET we mean LET in water, i.e., the energy lost in an infinite volume.) The RAD dynamic range covers the LET range from 0.2 to approximately 1000 keV/ μm . RAD also measures neutrons and γ -rays with energies from ~ 5 to 100 MeV using an approach similar to that discussed by Posner et al. (1995).

Due to energy constraints of the rover power system, it was necessary to design RAD with the capability to operate autonomously, with a duty cycle typically less than 100 %.

Fig. 1 RAD energy range and coverage by particle type. Stopping particle energy ranges for charged particles are shown in solid colors

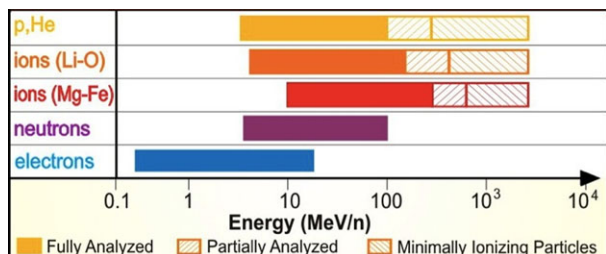


Table 1 RAD resources

Resource	RAD instrument
Mass	1.56 kg
Power	4.2 W (operating), 0.1 W (sleep mode)
Typical data volume	400 kB/day
Volume	240 cm ³

Consequently, RAD is designed to take observations for a configurable duration, and then sleep for some time (also configurable) before resuming data acquisition. The wake/sleep cycle repeats indefinitely until RAD is commanded otherwise. Scientifically, the ability of RAD to identify the onset and time profile of SEP events drives the need for an hourly observation cadence (discussed further in Sect. 2.1.2). Thus, during nominal operations, RAD takes observations roughly 16 minutes per hour, followed by 44 minutes of sleep time. RAD stores its data internally, with data from each observation stored in a single packet. RAD will then transfer data to the rover, which will nominally send it to Earth via telemetry, once per day. The observation cadence can be adjusted autonomously when the trigger rate exceeds a pre-defined threshold, thereby going into “Solar Event” mode. When this occurs, RAD observations will be shorter with a higher duty cycle (roughly 50 %). The cadence change is autonomous since there is not sufficient time for commanding from Earth once a SEP event starts.

The primary science objectives of the RAD investigation are:

- To measure energetic particle spectra at the surface of Mars;
- To measure dose and determine dose equivalent rates for human explorers on the surface of Mars;
- To use these measurements to enable validation of Mars atmospheric transmission models and radiation transport codes;
- To provide input to the determination of the radiation hazard and potential mutagenic influences to life at or just below the Martian surface;
- To provide input to the determination of the chemical and isotopic effects of energetic particles on the Martian surface and atmosphere.

The RAD design is driven by the need to address the first three goals (important for future human exploration), within the severe constraints on mass, volume, power, and telemetry of the MSL mission. The last two goals are interrelated, and can be addressed by using the science data products that RAD will already provide. Both goals pertain to use of RAD science data in models to answer life science, geology, or chemistry questions relevant to other investigations on MSL. These parameters are listed in Table 1.

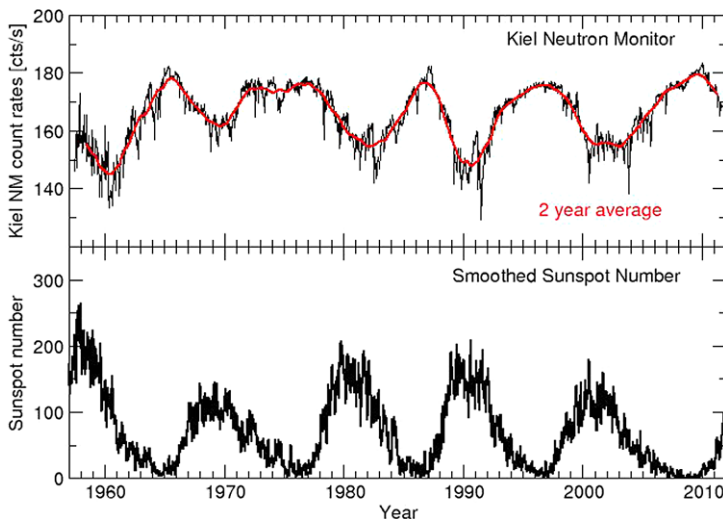


Fig. 2 Solar cycle modulation and anti-correlation of GCR flux with solar activity. Shown are observations from the ground-based Kiel neutron monitor (*top*), which are indicative of the GCR flux, and smoothed sunspot number (*bottom*)

2 Overview of RAD Science Objectives

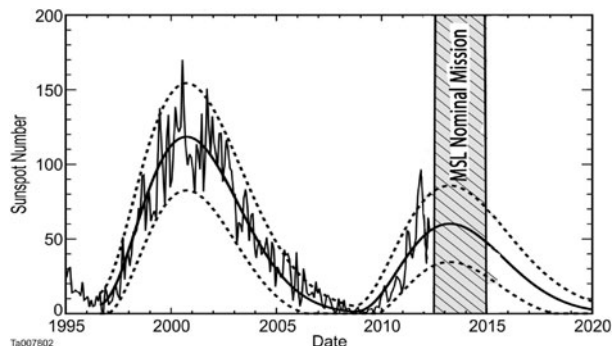
2.1 Characterizing the Energetic Particle Spectrum on Mars

Measurement of the composition and intensity of GCRs, SEPs, and their interaction products for the first time on the surface of Mars is the primary objective of the RAD investigation. The charged and neutral particle spectra on the surface of Mars are functions of both the incident flux and the effects of transport through the atmosphere and top layers of soil. Providing “ground truth” observations also enables the ability to test radiation transport models.

2.1.1 Galactic Cosmic Rays (GCRs)

As mentioned above, the ionizing radiation environment on the surface of Mars is determined by the GCRs and SEPs that impinge on the thin atmosphere. GCRs are high energy particles (10 MeV/nuc to 10 GeV/nuc and above) thought to be accelerated by supernovae shocks outside the heliosphere. The intensity and composition of GCRs observed in the inner heliosphere varies with solar modulation, typically on time scales of the solar cycle. The composition varies slightly, ranging from 85–90 % protons, 10–13 % helium, about 1 % electrons, and about 1 % heavier nuclei (Reedy and Howe 1999; O’Neill 2010). The effects of solar modulation are illustrated in Fig. 2. The observed 15–30 % variations in the GCR flux as a function of the solar cycle are anti-correlated with solar activity. A full explanation of the phenomenon in terms of fundamental physics remains elusive (Chowdhury et al. 2011). Rigidity is one of the important variables; since it depends on the charge-to-mass ratio (Z/A) of the incident ion, the flux of protons ($Z/A = 1$) is modulated more than are fluxes of other ion species ($Z/A \sim \frac{1}{2}$). Rigidity is also inversely proportional to momentum, so fluxes at low energies are more modulated than at high energies. For example, the Badhwar-O’Neill model (O’Neill 2010) gives a flux of 200 MeV

Fig. 3 RAD observations during the nominal MSL mission will coincide with the peak of the next solar cycle, as shown superposed on a current prediction of Solar Cycle 24 (Hathaway 2011)



GCR protons that is approximately a factor of 3 larger in 2010 (very weak modulation) than in 2002 (strong modulation). A comparison of the 200 MeV/nuc helium fluxes in the same time periods shows a difference of approximately a factor of 2. RAD observations during the nominal MSL mission will coincide with the peak of the next solar cycle (cycle 24), as shown in Fig. 3.

The deep and prolonged minimum in the descending phase of Cycle 23 produced the highest GCR fluxes yet recorded, including a flux of iron ions (possibly the most biologically hazardous particle in space, Cucinotta and Durante 2006), nearly 20 % higher than observed in the previous solar minimum (Mewaldt et al. 2009). Thus, GCR observations of the next solar cycle (both maximum and minimum) are of significant interest, and RAD will provide key measurements for comparison with other instruments operating during this time.

Because of their high energies, the large majority of GCRs pass through the Martian atmosphere, and under typical circumstances GCRs are the dominant source of ionizing radiation at the surface (with brief periods when large SEP fluxes reach Mars and may be dominant, Townsend et al. 1991). GCRs are also responsible for the production of secondary particles via nuclear and electromagnetic interactions in the atmosphere and regolith. GCR mean free paths for nuclear interaction are dependent on particle energy and mass, with typical values of 20 g cm^{-2} , which is similar to the thickness of the Martian atmosphere. It is these interactions, as well as the incident flux itself, that transport models—discussed further in Sect. 2.3—must accurately simulate if the radiation environment is to be accurately assessed.

To get a sense of the importance of secondary radiation on the surface, it is useful to consider the analogy to ionization in the Earth's atmosphere (Bazilevskaya et al. 2008) caused by GCRs. On Earth, ionization increases with atmospheric depth, reaching the “Pfotzer maximum” (Pfotzer 1936), at about 20 km above sea level, before it decreases due to absorption of the primary radiation. This maximum is caused by particle showers initiated by interactions of high-energy GCR particles with the atoms in the atmosphere. On Earth, the column depth of atmosphere above 20 km is on the order of 100 g cm^{-2} , substantially greater than the average column depth of the entire Martian atmosphere. The Pfotzer maximum on Mars therefore occurs a few tens of cm below the surface. However, it is a broad maximum, and the column depth of the atmosphere at the Martian surface is similar to the column depth at an altitude of 30 km on Earth. At this altitude, and at the Martian surface, the charged particle flux is still greater than in open, unshielded space (as can be seen for the lowest cutoff rigidities in Fig. 2 of Bazilevskaya et al. 2008). Thus the thin Martian atmosphere actually increases the surface flux of ionizing particles compared to the case of a planet or moon with no atmosphere. This increase in flux does not lead to an increase in dose equivalent

(and hence risk to biological organisms) at the surface compared to free space, because a large fraction of heavy ions with high biological effectiveness undergo fragmentation into lighter, less damaging ions as they traverse the atmosphere.

The analogy to high altitudes on Earth does not entirely hold, as the interactions of GCR in the top meter or so of Martian soil produces a non-negligible “leakage” flux of neutrons, which have been measured in orbit by instruments on Mars Odyssey (Boynton et al. 2004). Characteristic neutron and γ -ray fluxes observed as *Odyssey* orbits Mars have provided strong evidence for large deposits of sub-surface water ice (Mitrofanov et al. 2002; Boynton et al. 2002). Preliminary estimates of the neutron dose rates in Mars orbit have been made (Tretyakov et al. 2009) and are reportedly about 1 $\mu\text{Sv}/\text{hour}$, or 0.01 Sv/year at *Odyssey*’s altitude, 400 km above the surface.

Finally, it should be noted that Mars lacks a planet-wide magnetic field, so there is no shielding comparable to that provided by the Earth’s magnetosphere. An incoming GCR or SEP sees a maximum field strength of about 40 nT in localized regions (Luhmann et al. 2007), too little to cause significant deflection in the trajectories of the particles of interest here.

2.1.2 Solar Energetic Particles (SEPs)

High energy SEPs are produced in the solar corona as a result of high energy processes associated with flares, coronal mass ejections (CMEs) and their corresponding shocks. Flux enhancements over background plasma and cosmic ray levels occur in the energy range from ~ 1 keV to several GeV for the most severe solar storms, and fluxes can vary by more than 3–5 orders of magnitude on time scales of hours to days (Posner and Kunow 2003; Dorman et al. 2003), as illustrated by GOES 13 observations of the March 7, 2012 SEP event in Fig. 4. SEP fluxes are typically dominated by protons, but composition can vary substantially (Cane et al. 2010). Most SEP ions have energies below 100 MeV/nuc and are therefore not able to penetrate to the surface of Mars, but fluxes are highly variable from event to event, and in some instances there are significant fluxes above 100 MeV/nuc. In these events, a significant flux of SEPs will reach the surface, and in all events, secondary neutrons produced by SEPs in the atmosphere can reach the surface. We expect that hard-spectrum events may, for relatively brief periods, occasionally overwhelm the GCR radiation at the Martian surface (Townsend et al. 1991).

The flux of SEPs arriving at Mars is likely to be different than in near-Earth space since the magnetic connection between the Sun and Earth is likely to be different from that of the Sun and Mars. The extreme cases are the months after conjunction, when Mars sees the back side of the Sun, and the months after opposition, when the two planets may be on the same Parker spiral. Therefore a SEP event seen at Earth may not be seen at Mars, and vice-versa, whereas other events are seen at both planets even when they are at or near conjunction. Catalogues of SEP events observed in Mars orbit by MGS and *Odyssey* are available (Zeitlin et al. 2010a; Delory et al. 2012), and demonstrate these effects. Correlation of SEP observations on the surface of Mars with measurements made at other points in the heliosphere is also a key investigation objective.

2.2 Determining the Radiation Dose Rate for Future Human Exploration of Mars

2.2.1 Model Predictions

RAD will make the first direct measurements of the radiation environment on the surface of Mars, which is essential for planning future human missions. Future astronauts conducting

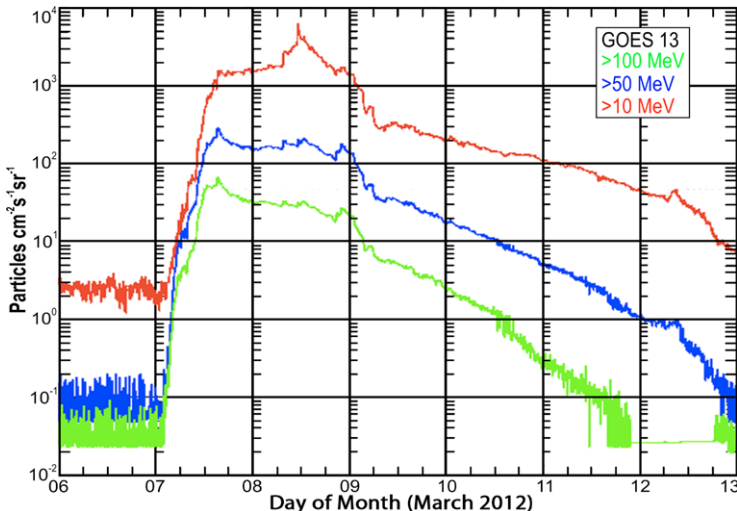


Fig. 4 Solar Energetic Particle Event from March 7, 2012. Shown are GOES proton fluxes for three different energies as a function of time. RAD's hourly observing cadence was chosen to enable observation of the onset and evolution of the structure of SEP events similar to the one shown in the figure

Martian surface operations will experience a continuous exposure to GCR radiation, and potentially large but short-duration exposures from SEPs. Neglecting the effect of the atmosphere for a moment, the dose rate on the surface of Mars should be less than that in interplanetary space by a factor of two. This is true on the surface of any planet or moon, simply because the GCR flux is isotropic, and on a surface, half of the 4π steradian field of view is blocked. On Mars, the atmosphere—consisting of approximately 16 g cm^{-2} of CO_2 on average—provides some shielding against GCR heavy ions. For instance, the mean free path of a high-energy ^{56}Fe ion in CO_2 is about 12 g cm^{-2} , so that roughly 25 % of incident ions reach the surface; the rest fragment into lighter ions. The LET of GCR iron ions is 150–200 keV/ μm , near the peak of the quality factor, Q (ICRP 1991), so that their contribution to dose equivalent in unshielded space is significant. Fragmentation of these ions (and other heavy ions) in the atmosphere therefore reduces their contribution to the dose equivalent at the surface, so in this sense the Martian atmosphere can be said to provide some shielding. However, the atmosphere does not shield the surface from the high-energy protons that comprise the majority of the GCRs, and in fact increases the dose rate associated with low-LET particles as well as the production of additional high LET particles such as neutrons.

Several predictions for the radiation environment that RAD will measure have already been made (Wilson et al. 1999; Clowdsley et al. 2001; Cucinotta et al. 2002; Saganti et al. 2004; De Angelis et al. 2006; Ehresmann et al. 2011). At the surface, the dose equivalent rate from GCRs and their secondary products is predicted to be 0.2–0.3 Sv/yr, depending on altitude (Saganti et al. 2004). (Model assumptions include 22 g cm^{-2} depth of CO_2 at zero surface elevation for solar minimum conditions, and no contribution from backscattered neutrons.) This dose equivalent rate is about three orders of magnitude greater than that from cosmic rays at sea level on Earth. It should be noted that primary cosmic rays very rarely reach the Earth's surface, due to shielding from the magnetosphere and $\sim 1000 \text{ g cm}^{-2}$ of terrestrial atmosphere. Thus, RAD data will provide the first “ground truth” observations against which these predictions can be compared.

2.2.2 Human Mission Considerations

The GCR flux is lowest at solar maximum, so if one aims to minimize GCR exposure (and the associated large uncertainties in biological effect), missions to Mars should go at solar maximum. However, this is also when the probability of large SEP events is greatest. It has been shown that dose equivalents to the skin and lens from large SEP events can, even under 10 g cm^{-2} of shielding, approach annual exposure limits (Townsend et al. 1991). This is about the depth of shielding provided by the Martian atmosphere at elevations of 6–8 km according to Saganti et al. (2004), depending on the choice of atmosphere model. There is even less shielding at higher elevations such as Elysium Mons. For reference, the Apollo spacecraft had only about 5 g cm^{-2} of shielding (on average).

The Design Reference Architecture (Drake 2009) for a human mission to Mars takes about 1000 days, with a surface stay of about 500 days. Much of the accumulated dose on such a mission would be received in transit. Overall, astronauts are expected to receive about 1 Sv (Cucinotta and Durante 2006) of dose equivalent from GCR, depending on shielding thickness. (SEP events will add even a higher exposure to the total, up to several Gy in rare cases.) Presently, career radiation exposure limits for fatal cancer risks for exploration missions, including a Mars missions, correspond to a 3 % probability of radiation exposure induced death (REID). Because of the large uncertainties in projecting cancer risks, NASA has an auxiliary requirement of satisfying the 95 % confidence level in the estimate of fatal cancer risk. The allowable exposure is a function of the astronaut's age, gender, and smoking history (Cucinotta and Chappell 2011). The most recent human epidemiology data suggest more restrictive dose limits compared to prior estimates (NCRP 2000). Central estimates of effective dose limits range from ranges from 0.7 Sv for a 30-year-old female never-smoker to 1.2 Sv for a 50-year-old male never-smoker with reduced values (more restrictive) for former smokers (Cucinotta and Chappell 2011; Cucinotta et al. 2011). The 95 % confidence levels reduced these values by more than 3-fold compared to the central estimate. It is important to emphasize that the uncertainties are larger for Mars missions compared to LEO missions because of the higher fraction of the exposure due to GCR heavy ions. Given these expected exposures, it is important that measurements, such as those to be made by RAD, be carried out well in advance of any future manned missions in order to properly assess the safety risks and to develop potential mitigation strategies (NRC 2008).

2.2.3 Measurement Requirements for Future Human Exploration

Accurate and complete dosimetric measurements are of value by themselves and will also facilitate model comparisons. Given the many sources that contribute to the radiation environment on the surface of Mars, the basic requirements for a radiation detector on the surface of Mars are:

- A wide dynamic range for charged particle measurements;
- Resolution sufficient to identify charged particles by species;
- Sensitivity to neutral particles.

To fully measure the charged-particle dose, the dynamic range of the instrument must cover everything from minimum-ionizing charged particles ($\text{LET} \sim 0.2 \text{ keV}/\mu\text{m}$) to slow heavy ions ($\text{LET} \sim \text{several hundred keV}/\mu\text{m}$). Measurement of the LET spectrum allows not only for measurements of dose, but for calculation of dose equivalent (after conversion of dE/dx in silicon to LET in water and applying the appropriate quality factor, which is a measure of biological efficiency).

Determination of LET spectra is important and necessary in the standard paradigm of risk assessment for mixed radiation fields. However, identification of ions by species (or at least by group, e.g., C–N–O) is required if one is to use the new risk assessment tools developed by NASA (Cucinotta et al. 2011). This new approach estimates the risk per particle using the quantity Z^{*2}/β^2 , where Z^* is the effective ion charge number and β its velocity divided by the speed of light, and distinct risk coefficients for light ($Z \leq 4$) and heavy particles ($Z > 4$). The resulting quality factors are then a function of Z and E (Cucinotta et al. 2011). This puts new emphasis on the ability of detectors to measure particle spectra, as opposed to simply LET spectra (as could be done with a comparatively simple Tissue-Equivalent Proportional Counter or TEPC). As an illustrative example, consider a relatively low-energy proton (65 MeV) and high-energy helium ion (600 MeV/nuc) with equal LET of about 1 keV/ μ m. The proton has relatively low velocity and therefore short range (about 3.6 cm), and will not contribute to the dose at depth in tissue (unless it was produced within tissue by either slowing down or nuclear interaction). In contrast, a helium ion with the same LET has comparatively long range (~ 155 cm), and therefore does contribute significantly to the dose at depth. At very high energies ($E > 1$ GeV/nuc) the LET of particles remains relatively constant, however the microscopic energy deposition or track structure of particles continues to broaden, reducing their biological effectiveness. The mixed-field quality factor Q, which is defined to depend only on LET, fails to account for such effects. However, the recent NASA quality factors are derived from track structure considerations (Cucinotta et al. 2011) and lead to distinct particle detection considerations that can be addressed by RAD.

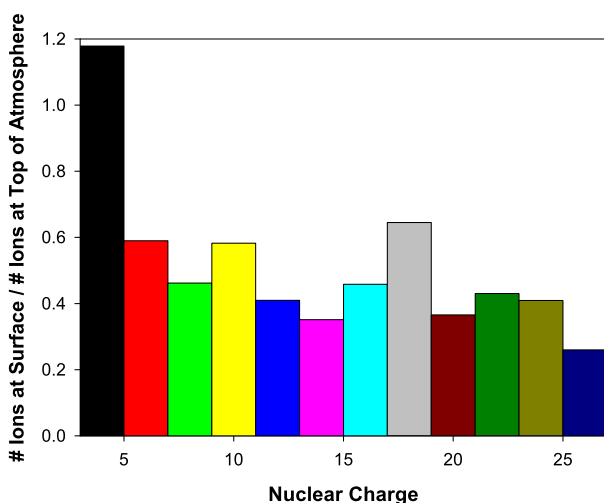
Finally, the contributions to dose and dose equivalent from neutral particles must also be measured. RAD has these capabilities, as described in detail in Sect. 3.1.2. As part of its nominal event processing, RAD creates a set of dosimetry histograms. These data can, with minimal processing on Earth, be turned into dose rate time series for the B detector (silicon, primarily sensitive to charged particles) and for the E detector (plastic, with comparatively high sensitivity to neutral particles, especially neutrons). We expect these to be among the most useful RAD data products.

2.3 Validation of Models of Radiation Transport Through the Martian Atmosphere

Space radiation transport models play a central role in radiation risk assessment for astronauts, and will continue to do so in the future (Wilson et al. 2001). There are two inescapable reasons for this. First, the complexity of the underlying physics—particularly the nuclear interactions—is such that not all of the ingredients of a model can be taken from measurements. Many nuclear cross sections have not been measured and must be estimated, and this lack of data may introduce significant biases and/or uncertainties (Townsend et al. 1990). Second, standard radiation protection guidelines used by NASA require knowledge of dose equivalent at points inside the body. This is only possible with modeling, and so the radiation fields that are known or calculated (with uncertainties) to exist in certain environments must be propagated, or transported, to specific locations, with the addition of more uncertainties due to the limitations of the models. The model uncertainties increase as the depth of material being modeled grows. In addition, atmospheric conditions on Mars, including seasonal changes in composition due to condensation of CO₂ and variable regolith properties will modulate the surface radiation environment further. (The factors that account for biological effect have even larger uncertainties.)

Accelerator-based validation of transport models of various codes is valuable but is not an adequate substitute for validation in real and more complex flight environments, such as on the surface of Mars. Previous work in this area has focused on providing a nuclear frag-

Fig. 5 Transport calculation based on the NUCFRG2 nuclear cross section model, showing the number of GCR heavy ions ($Z > 2$) at the Martian surface divided by the number incident, grouped by charge pairs



mentation database (Zeitlin et al. 2010b) with the aim of improving this aspect of transport codes. NASA uses the HZETRN model (Wilson et al. 1995) to calculate astronaut exposures. HZETRN is a fast analytic code, but it is known to lack physics details simulated by other codes such as FLUKA (Fassò et al. 2003), GEANT4 (Agostinelli et al. 2003), and MCNPX (Waters et al. 2007).

All transport codes that simulate GCRs or SEPs must start with some underlying assumptions about the flux; HZETRN, for example, uses the 2002 version of the Badhwar-O'Neill GCR model and has a small number of representative SEP events available. Other codes use static models or require the user to provide input spectra (Battistoni et al. 2008). Accurate measurements from MSL-RAD in the Mars surface environment, with a time-varying atmosphere, will provide an excellent basis for evaluating the strengths and weaknesses of these models. However it is important to note that RAD data can only be tested against a complete model, i.e., one that includes both a model of the free-space GCR (or SEP) fluxes combined with a transport model of the Mars atmosphere.

Figure 5 shows results from a transport calculation using a relatively simple one-dimensional Monte Carlo code (Zeitlin et al. 1996; O'Neill 2010) that simulates nuclear fragmentation using NUCFRG2 cross sections (Wilson et al. 1994) and ionization energy loss. The flux of heavy ions (charge $Z > 2$) predicted by the Badhwar-O'Neill GCR model (using a modulation parameter typical of solar maximum) was transported through 16 g cm^{-2} of CO_2 (a representative column mass at the surface of Mars near the 0 m MOLA (Mars Orbiter Laser Altimeter) datum). The figure shows the ratio of the number of ions at the surface to the number of ions incident. There is a net depletion of heavy ions, and net increases of lighter ions and especially protons (not shown in the figure). Some heavy ion species are preferentially re-populated by feed-down from fragmentation of heavier ions. Neutrons, muons, and pions (not simulated here) are also produced in the atmosphere and can reach the surface. Figure 6 is also the result of a transport model calculation done using the same code that was used to produce Fig. 5. Here, we emphasize the large contributions to dose equivalent from heavy ions and their fragmentation products. Considering that the mostly highly-charged ions contribute less than 0.05 % of the charged-particle flux, the fact that they contribute nearly 40 % of the dose equivalent is remarkable.

The effects of atmospheric shielding, and the production of secondary particles, depend on the total column mass above, and therefore vary with altitude, time of day, and sea-

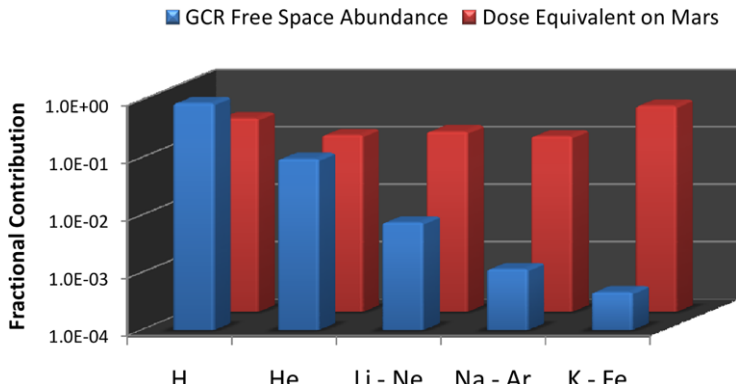


Fig. 6 Despite their low abundance, heavy ions and the secondaries they produce contribute significantly to the dose equivalent on the surface of Mars

son; these effects were not simulated in making Fig. 5. Other radiation transport model calculations (see the examples cited above) have also incorporated average, static bulk properties of the Martian atmosphere. Although GCMS (Haberle et al. 1993) reproduce many aspects of the atmosphere, dust distribution, dust optical properties, seasonal pressure cycle, and thermal tide dynamics are challenging to simulate. As described above, greater atmospheric mass offers increased shielding from primary particle radiation in terms of dose equivalent, along with an increased flux of low-LET secondary particles. Atmospheric pressure may vary seasonally by as much as 25 % or $\pm 2 \text{ g cm}^{-2}$ (Hess et al. 1979). Daily thermal tides can modulate the atmospheric surface pressure by $\pm 5 \%$ (Hess et al. 1977; Schofield et al. 1997), and occasional large transient variations are observed to modulate the atmospheric surface pressure up to 15 % (Tillman 1988). Not only does seasonal condensation of CO₂ decrease the overall column mass, it changes the fundamental composition of the atmosphere by effectively enriching of the dominant noncondensable gases N₂ and Ar (Sprague et al. 2004, 2007), which could affect the transport interactions. Hourly observations by RAD, in conjunction with pressure measurements from the Rover Environmental Monitoring Station (REMS) (Gómez-Elvira et al. 2008), will quantify these effects on the surface radiation environment.

Finally, the validation of radiation transport models requires spectral information, i.e., particle flux vs. energy for several different particle types or groups. It is necessary but not sufficient to compare dose and dose equivalent rates to model predictions, as there can be fortuitous agreement. Hypothetically speaking, an unknown inefficiency in a measurement could lead to a reported dose rate lower than the true dose rate; this might accidentally agree with one model or another, but only because both would be erroneous. More rigorous tests must be performed. RAD has resolution sufficient to identify protons, helium ions, ions in the C–N–O group, ions in the Ne–Mg–Si group, and heavier ions such as Fe. RAD will also provide, with broad bins, neutron spectra. In all cases, measured fluxes of ions or groups of ions will be compared to model predictions.

2.4 Radiation Hazard for Past and Present Life on Mars

The radiation effects on potential indigenous Martian life forms (past and present) are unknown, but most current studies assume that life elsewhere will be based on polymeric

organic molecules (Pace 2001), and will in an overall sense, share with terrestrial life the vulnerability to energetic radiation. Thus the risks to extant organisms are assumed to be analogous to the risks to future human explorers. Energetic particles ionize molecules along their tracks, creating OH and other damaging free radicals. More specifically, energetic particles can modify or even break DNA strands within cells, with the surviving cells becoming cancerous (NRC 2008). While Martian life may not be based on DNA, most astrobiologists assume that it will require some system of heredity based on large polymeric organic molecules (Grinspoon 2003). Thus it may have similar vulnerability to energetic radiation.

2.4.1 Estimating Lethal Depth for Life Below the Mars Surface

RAD will quantify the flux of biologically hazardous radiation at the surface of Mars today, and measure how these fluxes vary on diurnal, seasonal, solar cycle and episodic (flare, storm) timescales. These measurements will allow calculations (with validated transport models) of the depth in rock or soil to which this flux provides a lethal dose for known terrestrial organisms. Through such measurements, we can learn how deep life would have to be today to be protected. Even the resistant organism *D. radiodurans* would, if dormant, be eradicated in the top several meters in a timespan of a few million years (Pavlov et al. 2002). However, supposed recurring climate changes in the post-Noachian era, due to variations in the planetary obliquity on time scales of several hundred thousand to a few million years (Laskar et al. 2002), could lead to recurring periods of biological activity of these otherwise dormant life forms. In this case, it is hypothesized that accumulated radiation damages could be repaired and the “survival clock” of such life form could be reset to zero for the next dormant phase (Mileikowsky et al. 2000), which could in turn lead to possible survival to present times. In either case, characterizing and understanding the radiation environment on the surface today is a necessary first step.

An additional threat to potential life forms is the existence of strong oxidants that destroy organic molecules in the near surface environment of Mars; this hypothesis was advanced to explain the disparate results from the Viking LR (Labeled Release) and GCMS (Gas Chromatograph Mass Spectrometer) experiments (Zent and McKay 1994). Such oxidants, if they exist, may diffuse to a depth of a few meters (Bullock et al. 1994), sterilizing the top layer. However, the discovery of perchlorates at the Phoenix landing site (Hecht et al. 2009) further complicates the picture. If the Dartnell et al. (2007a) and Pavlov et al. (2002) analyses are correct, then sterilization by radiation occurs deeper in the soil, and will determine the minimum depth needed to drill to look for extant life, or signs of past life, on Mars today. Again, characterizing the radiation environment at the surface will provide a necessary benchmark to aid future investigation of these competing theories.

2.4.2 Extrapolating the Radiation Environment for Ancient Mars

While the idea of extant life existing today on Mars is controversial, the idea of life on Mars in the past is somewhat less so. The recent discoveries by the Mars Exploration Rovers (MER) and other orbital missions (e.g., Bibring et al. 2006; Christensen 2003; Fairén et al. 2009; Head et al. 2003; Squyres and Knoll 2005) of evidence for abundant surface liquid water in the past reinforces the widespread view that Mars, in the past, may have been a habitable planet. In seeking to understand the limits of surface habitability in the past on Mars, it is important to be able to accurately model the radiation environment during past epochs when surface water existed, the climate was more moderate, and presumably the atmosphere was substantially thicker than at present. Understanding how radiation interacts with the contemporary atmosphere permits the extrapolation of this interaction with the ancient, thicker atmosphere (Bullock and Moore 2007;

Forget and Pierrehumbert 1997; Johnson et al. 2003; Pollack et al. 1987). Although measurements of the current surface radiation environment cannot be directly related to the radiation environment in past epochs, estimates of the atmospheric column depths in previous epochs can be inferred using models of the early Martian climate (Haberle 1998; Haberle et al. 2003). Transport models (validated against current conditions as described above) can then be legitimately applied to make estimates of the radiation environment in those epochs (Dartnell et al. 2007b; Ehresmann et al. 2011).

It has long been speculated (Failla 1941) that radiation may be an important source of biological mutations, and as such may have been the dominant source of genetic diversity in the past on Earth. Presumably this would apply equally to other planets, including Mars. If life exists on Mars, the GCR-induced mutation rate is estimated to be comparable to the rate of spontaneous mutations on Earth (Yang et al. 1994). A thicker past atmosphere, required for a warm, wet early Mars, would have produced a somewhat different radiation environment than now exists, and presumably a lower radiogenic mutation rate. But, bearing in mind the analogy to the Pforzheim maximum on Earth, a moderately thicker atmosphere (say 100 g cm^{-2} column depth) may not be particularly beneficial from the standpoint of shielding the surface from GCRs. Any effort to understand the past radiation environment of Mars must begin with a thorough understanding of the role that the current atmosphere plays in modulating and altering the radiation from space. In Sect. 2.3, we outlined how the modern day radiation fluxes measured with RAD will be compared with surface fluxes calculated through atmospheric transport models. Once these models and our techniques are further validated (or refined) through comparison of present day model fluxes with atmospheric transport calculations, we will be able to use these same models to simulate the surface radiation environment at different times in the past, with appropriate variation of such input parameters as total atmospheric mass and entrained dust, according to published models of atmospheric history. Understanding the history of the atmosphere may well be further refined by observations made with other MSL instruments during the mission.

2.5 Chemical and Isotopic Effects of Radiation on the Martian Surface and Atmosphere

On geological time scales, an enormous fluence of high-energy charged particles (both primary and secondary) has interacted with, and possibly altered, the Martian regolith. If estimates of the present dose equivalent rate can be extrapolated back for as little as 10^7 years, the surface and shallow sub-surface have received on the order of a few million Sieverts (Sv) of radiation. This raises the possibility that ionizing radiation may have contributed significantly to the unique chemistry of the Martian surface.

2.5.1 Radiation Weathering and Relative Surface Ages with RAD

The surface of Mars provides unique conditions for studying the effects of space weathering on solar system bodies. Airless bodies experience a darkening and reddening of their surface, due to the combined effects of micrometeorite impacts and high energy particles (Hapke 2001; Chapman 2004). Both of these processes vaporize surface materials, which become coated with condensed vapor and very fine metallic Fe particles. It is the formation of these particles, smaller than the wavelength of light, in the top 10 nm of surface material that largely explains the optical effects of space weathering.

On Mars, sputtering-produced vapor deposition will also occur because attenuation of SEPs and GCRs by the atmosphere is minimal. However, impact vaporization is virtually absent, since Mars' atmosphere screens micrometeorites of the typical 10–100 μm size responsible for weathering the lunar surface. Therefore, measurements of the SEP and GCR

flux at the surface of Mars will enable an interpretation of high-energy particle weathering of the Martian surface, without the addition of micrometeorite-induced melting and vaporization. This is just the opposite case from Mercury, where the weak magnetic field deflects solar wind particles, while leaving the surface vulnerable to micrometeorite impacts. A comparison of the properties of the regolith of Mars and Mercury will therefore provide a more detailed understanding of the individual physical processes involved in space weathering. Understanding how surface materials on Mars are altered by energetic particles will be useful for separating out the relative effects of dust and high-energy particles on space weathering of airless bodies.

Space weathering is a slow process, and is hence an independent chronometer of solar system surfaces. Hapke (2001) calculated that the timescale for space weathering in the asteroid belt, due only to SEPs, should be about 50,000 years. However, spectral studies of young asteroid families show that realistic space weathering timescales in the asteroid belt, including galactic cosmic rays, solar energetic particles, and micrometeorites is on the order of several million years (Chapman 2004). On Mars, where only one process is at work, the timescale for space weathering is likely to be longer.

Vaporization and deposition by high-energy particles alters the surface of Mars in ways that are not understood yet, but are likely to affect the optical properties and small-scale structure of surface materials. One possible contributor to the rinds seen on Martian rocks is surface radiation interactions. The CheMin instrument (Blake et al. 2009) on MSL will probe the small-scale structure of surface material, looking for evidence of metallic particles and other signatures of high-energy particle interactions. RAD will supply the time dependent and integrated energy spectra of the high-energy particles that weather Mars' surface. Models of the interaction of incoming high-energy particles and the regolith can be used to predict the formation rate of reduced Fe particles. This new Mars surface chronometer can be calibrated by space weathering timescales determined for Mercury, the moon, and the asteroid belt, which all have different high-energy particle and micrometeoroid fluxes.

2.5.2 Exchange of CO₂ Between the Atmosphere and Regolith

GCR interactions in the atmosphere and within the regolith provide a source of ¹⁴C via nuclear reactions (Jakosky et al. 1996). ¹⁴C in turn, decays with a well-known half-life. Thus, radiation emplaces time-dependent tracers in the atmosphere and regolith. As CO₂ moves from the atmosphere to the regolith and returns, the carbon isotopes are fractionated. If the production rate of ¹⁴CO₂ within the regolith and atmosphere are known, then the steady-state mixing ratio ¹⁴CO₂/¹²CO₂ in the atmosphere indicates the relative amounts of CO₂ in the atmosphere and regolith. Because the half-life of ¹⁴C is 5730 years, the exchange of CO₂ between the atmosphere and regolith on timescale of 1000s of years is also recorded in the ¹⁴CO₂/¹²CO₂ ratio, if the quantity of CO₂ in the regolith is determined independently (i.e. Zent and Quinn 1995).

Jakosky et al. (1996) estimated the steady-state mixing ratio as 3.3×10^{-14} , but this number was determined by modeling GCR interactions with the atmosphere and regolith from the Los Alamos High Energy Transport (LAHET) Code System. The production rate of ¹⁴C within the regolith is orders of magnitude larger than in the atmosphere, and depends on the spectral flux of GCRs at the surface. At the same time, the flux of GCRs at the surface depends upon the attenuation of GCRs within the atmosphere. Direct measurements of GCR fluxes at the surface by RAD will validate the models of GCR atmosphere interactions, which are in turn used to determine the ¹⁴CO₂ production rates. The SAM (Sample Analysis at Mars) instrument (Mahaffy et al. 2012) will measure atmospheric ¹⁴CO₂ abundance,

enabling the RAD data to be used for understanding the size of the atmospheric and regolith CO₂ reservoirs, as well as exchange between these reservoirs in the past few thousand years.

3 Overview of the RAD Instrument

RAD consists of two parts, the RAD Sensor Head (RSH), and the RAD Electronics Box (REB), packaged together in a tightly integrated unit, as shown in Fig. 7(a). The RSH consists of a solid-state detector telescope with three silicon PIN diodes for charged particle detection and three scintillators that are used for both charged and neutral particle detection. The scintillators include a thallium doped cesium iodide crystal that stops some charged particles and efficiently detects gamma rays, a plastic scintillator (Bicron BC432m) primarily for neutron detection, and an anti-coincidence shield that allows us to veto charged particles entering RAD from the side or bottom. The RSH also contains the front-end read-out electronics. The REB includes three circuit boards: an analog board with a novel mixed-signal ASIC and a control FPGA, a digital board with a second FPGA to communicate with the rover, and a power supply and sleep-control electronics board which enables autonomous operation, independent of the rover. The hardware and firmware are described in the next two sections. A brief description of the model philosophy and calibration of RAD is discussed in Sect. 5, and a discussion of the predicted performance and a description of the expected data products is given in Sects. 6 and 7, respectively.

3.1 The RAD Sensor Head (RSH)

The RSH contains several particle detectors and associated front-end electronics (FEE). Three types of detectors are used to measure the radiation environment: 300 μm thick silicon p-i-n diodes or PIPS (Passivated Implanted Planar Silicon) detectors manufactured by Canberra [2006], an inorganic thallium-doped cesium iodide scintillator (CsI(Tl)), and plastic scintillators (Bicron BC-432m). Light from both the CsI(Tl) and BC432m scintillators is collected with silicon photodiodes that are identical in structure to the PIPS silicon diodes used to measure the deposited charge in the charged particle telescope. Figure 7(b) shows the detector arrangement schematically, as well as the principles of operation for charged and neutral particles. Identification of ion species at moderate energies is achieved with the dE/dx vs. E_{tot} method, used since the days of the IMP-1 satellite (McDonald and Ludwig 1964). The detectors are labeled from top to bottom as A, B, C, D, and E. The anticoincidence shield, labeled F, surrounds D and E. The orientation shown in Fig. 7(b) is preserved in the mounting of RAD to the MSL rover (Fig. 8). When the rover is on flat ground, the central axis of RAD is vertical, with the A detector at the top.

As mentioned above, all RAD signals are generated in silicon diodes, which produce charge either by direct ionization of the diode by a charged particle, or by collection of scintillation light. All signals are also handled in the same way: they are routed to charge-sensitive preamplifiers in the RSH, and outputs from the preamplifiers are passed to shaping amplifiers, also located in the RSH. The shaped signals are passed to the REB, where additional processing takes place. The FEE electronics will be discussed in more detail in Sect. 3.1.3 and the REB electronics will be discussed in Sect. 3.2. Below, we present a detailed description of the detectors themselves and their functions.

Fig. 7 (a) Cross section cartoon view of RAD showing the charged particle and neutral particle channels and electronic board layouts. (Not necessarily shown to scale.) (b) Schematic diagram of RAD illustrating the coincidence and anti-coincidence concepts. Particle paths shown in green are considered valid events, particle paths shown in red are rejected. (Not necessarily shown to scale.)

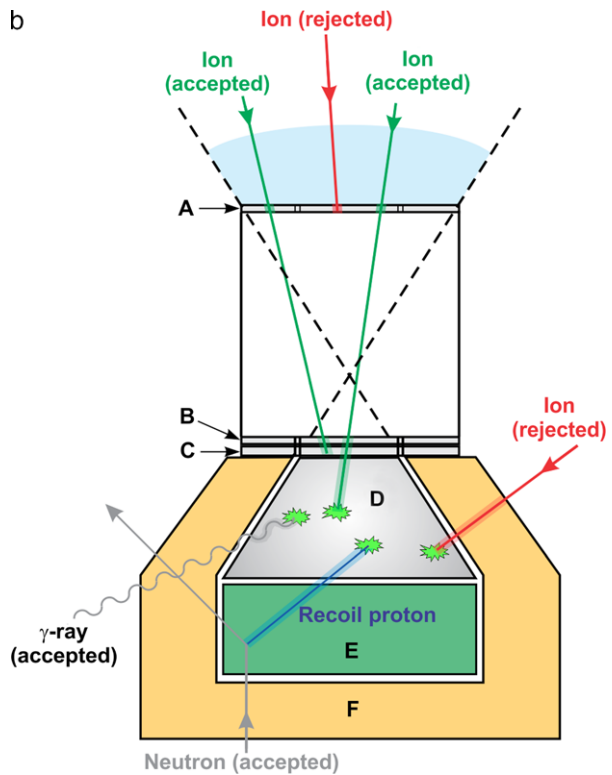
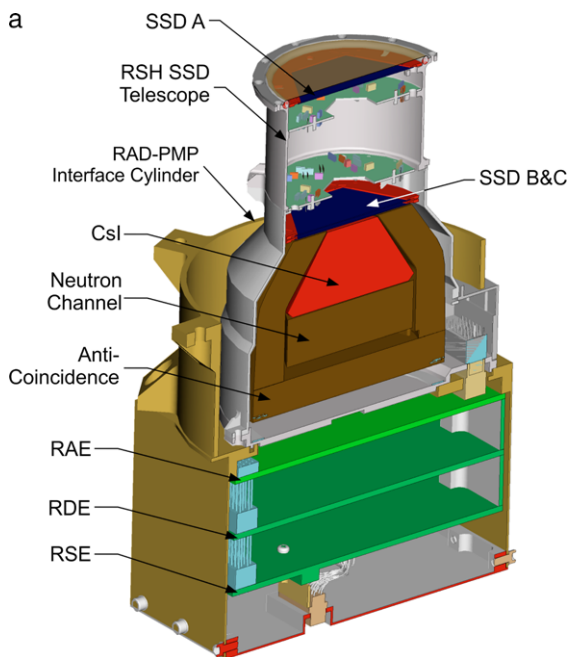
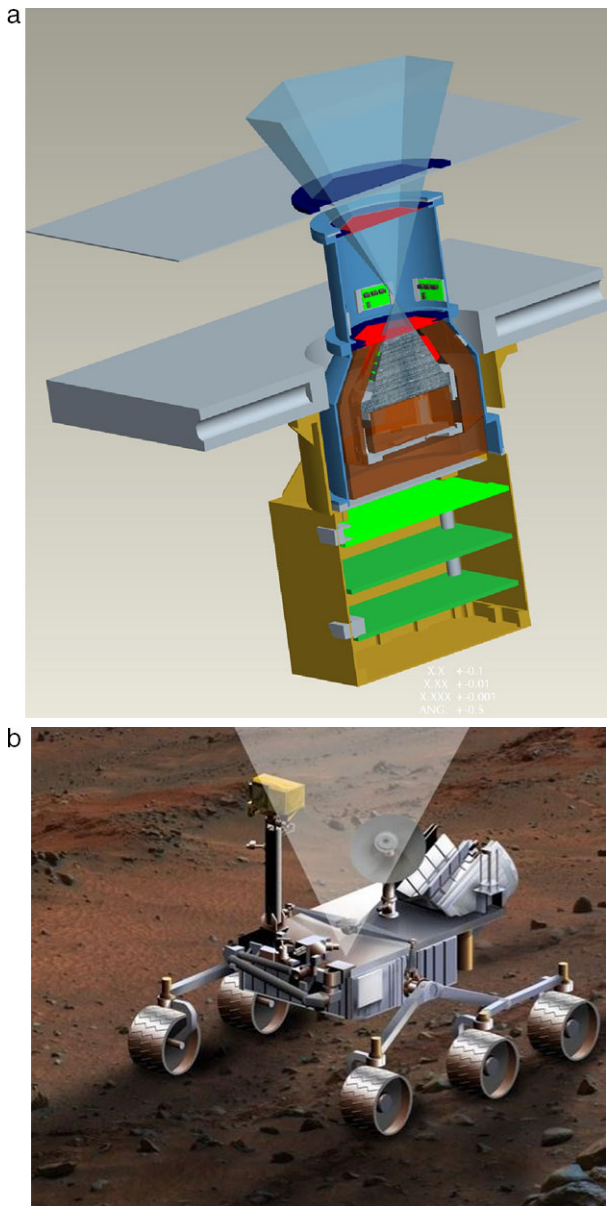


Fig. 8 (a) Cross section view of RAD mounted to the MSL Payload Mounting Plate (PMP).
(b) Cartoon view of the RAD charged particle telescope field-of-view



3.1.1 Charged Particle Detection

The Charged Particle Telescope The A and B detectors define the telescope geometry for charged-particle detection. Charged particles entering RAD from the top are measured in a view-cone of about 60° full opening angle, as illustrated in Fig. 7b. The A, B, and C detectors directly record the passage of energetic charged particles with charges Z from 1 to 26. Figure 9 shows the segmentation of these diodes. (We distinguish between the diodes themselves and detectors, which we define as particular segments of the diodes.) The

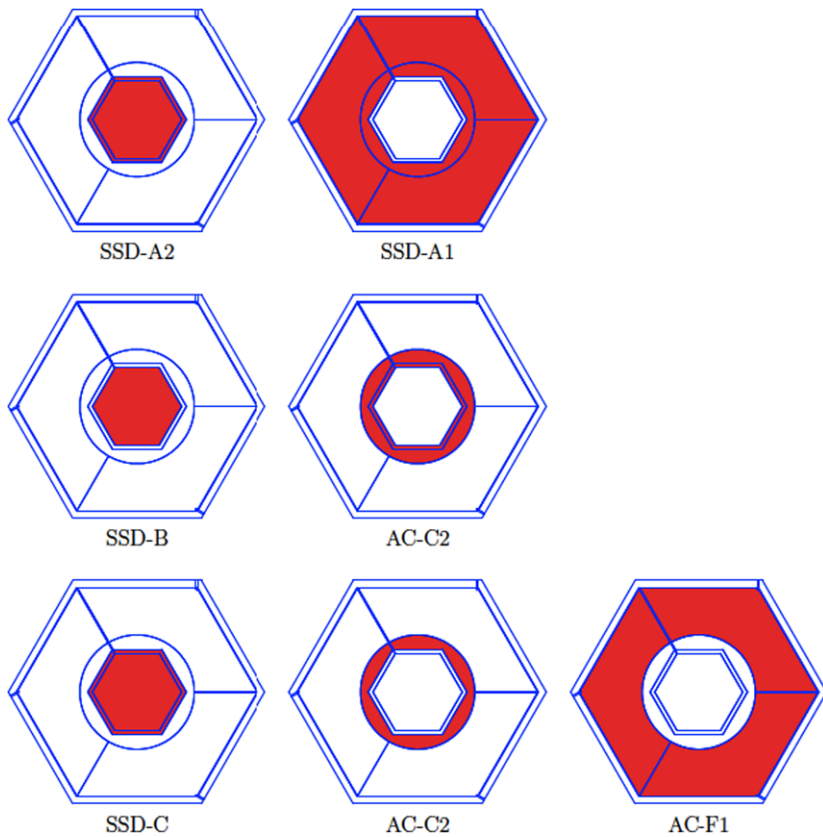


Fig. 9 Segmentation of the solid-state diodes in the RAD RSH. *Shaded areas* correspond to the active areas

A diode is split into outer and inner areas, defining detectors A1 and A2 respectively, with A2 consisting of the two innermost segments of the diode. The B detector consists of only the single innermost segment of the B diode. The B diode is 50 mm below the A diode, and the C diode is 1.4 mm below the B diode. The C detector is made up of the two innermost segments of the C diode. As shown in Fig. 9, the additional annular segment included in C makes it slightly larger than B so as to cover the full projection of the viewing cone defined by A and B. The outermost segments of the C diode are optically coupled to the upper part of the anticoincidence, known as the F1 detector. Some segments of the B and C diodes are ganged to form the “C2” detector, which completes the anticoincidence.

The radial split of the A detector limits the path length variation for particle trajectories through A2, and keeps the capacitance of A2 small. Both factors lead to better dE/dx resolution in A2 compared to A1. However the geometry factor of the telescope defined by A2·B is small (about $0.17 \text{ cm}^2 \text{ sr}$). So while the resolution of A1 is not as good as that of A2, the A1·B telescope geometry factor is larger (about $0.73 \text{ cm}^2 \text{ sr}$). A listing of geometry factors for various fields of view is given in Table 2. The last three entries apply when RAD is on the surface of Mars and radiation is incident only from one hemisphere; during MSL’s cruise to Mars, radiation is incident from all directions, so factors of 2 should be applied to these values. Detection efficiencies are not accounted for in Table 2; the values given are purely geometric.

Table 2 RAD geometry factors

Field of view	G ($\text{cm}^2 \text{ sr}$)	Comments
A1-B-C-D	0.73	Outer cone
A2-B-C-D	0.17	Inner cone, highest dE/dx resolution
(A1+A2)-B-C-D	0.90	Inner + Outer Combined
B	6.03	$G = \pi A$ for isotropic radiation
D	187	$G = \pi A$ for isotropic radiation
E	209	$G = \pi A$ for isotropic radiation

The D detector, made of CsI(Tl), is in the shape of a truncated hexagonal pyramid with a height of 28 mm. The shape is chosen to preserve the viewing cone of the telescope defined by the A1-B coincidence geometry. The D detector is an efficient γ -ray detector, but also has some sensitivity to neutrons. However, it is of particular importance in charged-particle detection since it stops ions with moderate energies, as described below. Nuclear interactions of heavy ions in D are fairly probable and result in detection efficiencies that decrease as the ion mass increases. For example, we estimate that a 1 GeV/nuc ^{12}C ion entering D will undergo a charge-changing interaction with about 15 % probability; the comparable number for a ^{56}Fe ion is about 20 %.

The E detector is a hexagonal prism, 18 mm deep, made of BC-432m. Its primary function is neutron detection and it also records energy deposited by some charged particles. Because it does not fully cover the charged-particle viewing cone, some charged particles hit A1, B, C, and D, but not E. Trajectories that go through A2 and B will, in the absence of large-angle scatters, also pass through C, D, and E.

Stopping and Penetrating Charged Particles Highly energetic particles penetrate the entire stack before they leave the detector at the bottom. Less energetic particles may stop in the stack. Hits above threshold in at least the first two detectors (A1 or A2, and B) are required for an event to be considered a charged particle. Thus a charged particle must have enough energy to penetrate the two thin windows above RAD, the A detector, and have enough residual energy to deposit at least 60 keV in B. This imposes a minimum energy of about 8 MeV for protons at normal incidence.

The D detector presents sufficient mass (12.6 g cm^{-2}) to stop some incident charged particles. Protons with kinetic energies up to 95 MeV at the top of RAD stop in D, as do iron ions with up to about 500 MeV/nuc. The E detector also stops a small percentage of charged particles. For stopping particles, we can determine the charge, mass, and energy. These are the “fully analyzed” particles in Fig. 1.

For charged particles with energies that are just sufficient to fully penetrate RAD, the mass presented by D can cause significant slowing. These particles will deposit large amounts of energy in E compared to highly-relativistic particles whose dE/dx changes very little in traversing RAD. Thus E can be used to determine the energy for a limited range of penetrating charged particles. Because E does not fully cover the viewing cone defined by A1 and B, we restrict this class of particles to those passing through A2 and B. For particles in this category, we can determine the charge and energy (“partially analyzed” as per Fig. 1).

As a practical matter, fully penetrating charged particles that exit RAD through the F2 detector cannot be distinguished from slightly less energetic particles that stop in F2. Our criterion for determining whether a particle penetrated is simply whether F2 recorded a hit. Thus the relatively rare particles that stop in F2 are treated as penetrating. The charge and

Table 3 RAD charged-particle identification capabilities

Particle type	Max. energy, stopping in D
Protons, ^4He	95 MeV/nuc
^{12}C	180 MeV/nuc
^{16}O	220 MeV/nuc
^{20}Ne	280 MeV/nuc
^{28}Si	300 MeV/nuc
^{56}Fe	500 MeV/nuc
Electrons	30 MeV

LET of penetrating particles can be determined, but neither mass nor total energy can be inferred from the dE/dx measurements.

For the ranges in which particle charges and energies can be determined, one can report a differential flux. For all higher energies, incident energy cannot be determined and it is only possible to report an integral flux. Table 3 delineates some of the important cases.

Neutral particle detection is inherently more complicated than charged-particle detection. The mass and volume allocations impose limits on the detection efficiency for neutral particles, at both low and high energies, as will be explained in the next section. Despite this, RAD is capable of measuring a significant share of the neutral-particle dose on the surface of Mars.

3.1.2 Neutral Particle Detection

Scintillator Readout Both the CsI(Tl) detector (D) and BC-432m scintillators (E and F) emit orange light at wavelengths (about 540 nm peak) that can be efficiently detected with silicon photodiodes. The photodiodes used for this purpose are identical in structure to the diodes that are used for A, B, and C, which directly measure the deposited energy of charged particles. Photodiodes were chosen to read out the RAD scintillators because they are extremely compact and low-mass. Using photodiodes also allows RAD to have only a single bias voltage supply, which operates at -70 V. Photodiode readout of D and E also allows the anticoincidence plastic to fit closely around the neutral-particle detectors. Photodiodes are glued to three of the six side faces of the D detector, and circuit boards containing preamplifiers are mounted on the other three faces. Similarly, the E detector has photodiodes glued to three of its six faces.

The D and E detectors are both, to different degrees, sensitive to γ -rays and neutrons. Any given neutral-particle event may register in either detector, or, in rare cases, in both. A maximum-likelihood inversion method has been developed (Köhler et al. 2011), using the response functions of both detectors (calculated with GEANT4 and anchored to RAD calibration data) to separate the neutron and γ contributions to the spectra recorded. The method has been demonstrated to work well for neutrons with energies up to 19 MeV, and recently-obtained calibration data will allow us to extend the method to neutron energies up to at least 80 MeV.

The depth of the D crystal is sufficient to contain secondary electrons produced by γ -rays up to 100 MeV with reasonable probability. Because it is made from a high-Z material, D is an efficient γ -ray detector. In contrast, the E detector is a low-Z material with approximately equal parts hydrogen and carbon, making it a comparatively inefficient γ -ray detector but a useful neutron detector. An incident neutron can interact with either carbon or hydrogen, but the interactions with hydrogen are most important as they produce recoil protons which

can in turn produce relatively large numbers of scintillation photons. Typically several interactions, on the order of 10, must occur in order for the neutron to transfer all of its energy to recoil protons. Most neutrons will therefore only deposit part of their energy in E. We estimate that for neutrons at normal incidence in the energy range 10–100 MeV, there is a (weakly energy-dependent) probability of 2–3 % for a detectable signal to be produced by one or more recoil protons. The minimum detectable neutron energy, about 5 MeV, is relatively high due to the photodiode readout, since diodes have no intrinsic gain. In practice this is not a problem, since a lower threshold would likely cause the readout to be overwhelmed with triggers generated by neutrons and γ -rays from the Radioisotope Thermal Generator (RTG) that powers MSL. At the other end of the energy spectrum, the probability for a recoil proton to escape from E and hit the anticoincidence shield is significant when the recoil energy exceeds about 45 MeV. This limits the detection efficiency for high-energy neutrons.

Anticoincidence System For events with energy deposited in D and/or E, it is necessary to distinguish between cases where the energy is deposited by a neutral particle and cases where the energy is deposited by a charged particle with a trajectory entirely outside the viewing cone of the charged particle telescope. The anticoincidence system surrounds the D and E detectors in order to perform this function. F1, the upper piece of anticoincidence plastic scintillator, is tapered at the top, and circular in cross section below the taper. The lower piece, F2, is in the shape of a nearly-circular disk. Both pieces are made of BC-432m, are 12 mm thick, and can be used to detect minimum-ionizing singly-charged particles. The final part of the anticoincidence is the C2 silicon channel. As can be seen in Fig. 9, this consists of annular segments of the B and C diodes. Valid neutral particle events are defined as those with energy deposits above threshold only in D and/or E (i.e., with no significant energy in F1, F2, C, or C2).

Three silicon photodiodes are glued to F2, while F1 is coupled to the outer segments of the C diode. F1 and F2 are optically coupled to each other, so that scintillation light is shared among the photodiodes.

An unavoidable effect in RAD's anticoincidence system (and other similar systems) is the limited efficiency for high-energy neutrons. For any given event, a high-energy neutron entering the E detector may transfer a large share of its energy to a recoil proton, giving the proton enough range to exit E and hit F. Such events are rejected since they cannot be distinguished from charged particles entering from the side or from below. If, however, a recoil proton produced in E enters the D detector, it will likely be stopped, resulting in a valid neutral-particle event topology (D-E coincidence).

3.1.3 Front-End Electronics (FEE)

The Front-End Electronics for each channel consists of a charge-sensitive preamplifier and a shaping amplifier. The electronics are designed to have very low noise and good stability over the wide range of temperatures that RAD will encounter. Figure 10 shows a block diagram of the FEE. The RSH produces seventeen output signals. Preamplifier outputs for the A1, A2, B, and C detectors are split, with each branch going into a shaping amplifier. Thus these four detectors account for eight of the analog signal outputs. Preamplifier signals from each of the three readout diodes for D, the three readout diodes for E, and the C2 detector are not split, that is, each goes to a single shaping amplifier. These account for another seven signals. The three F1 readout diodes have individual preamplifiers, the outputs of which are ganged at the input of a single shaping amplifier; the same pertains to F2, bringing the total number of output signals to seventeen.

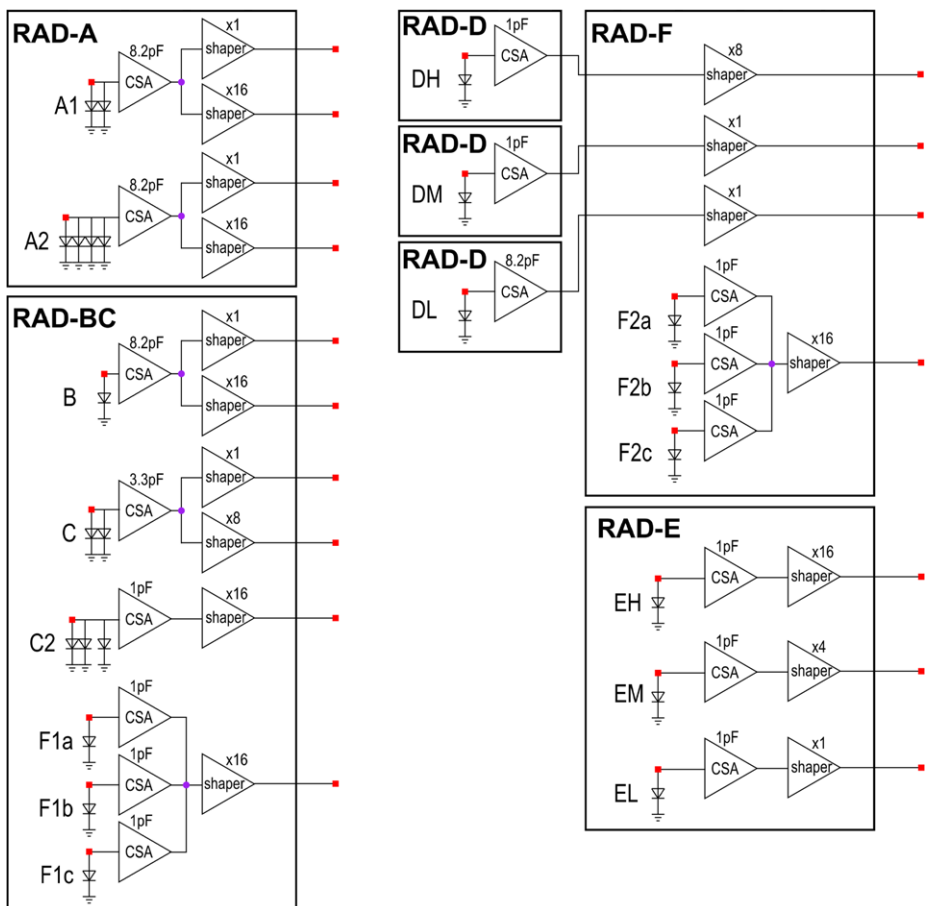


Fig. 10 Block diagram of the RAD Front-End Electronics

The A1, A2, and B channels have 8.2 pF feedback capacitors. This relatively large value is needed to avoid saturation of the readouts when slow heavy ions traverse the silicon telescope. Theoretically, the maximum energy deposition that can be seen without saturation in these channels is 650 MeV, which corresponds to the energy deposited by a ^{56}Fe ion with a kinetic energy of about 37 MeV/nuc. (The LET in water is about 1040 keV/ μm for such a particle.) Based on calibration data obtained with the flight hardware, actual gains are about 10 % larger than calculated based on a first-principles calculation that assumes nominal component values. Therefore the maximum LET without saturation is approximately 900 keV/ μm in water. The preamplifier for the C detector has a 3.3 pF feedback capacitor, giving it somewhat higher gain than the otherwise-comparable A and B channels. All A/B/C preamplifier outputs are split as per Fig. 10. In all cases the low-gain channels have unity gain. For A and B, $\times 16$ amplification is applied to the high-gain signals. For C, $\times 8$ amplification is applied to its high-gain channel. These signals are split again and undergo additional amplification in the VIRENA ASIC (on the RAE board, described below), providing both redundancy and larger dynamic range.

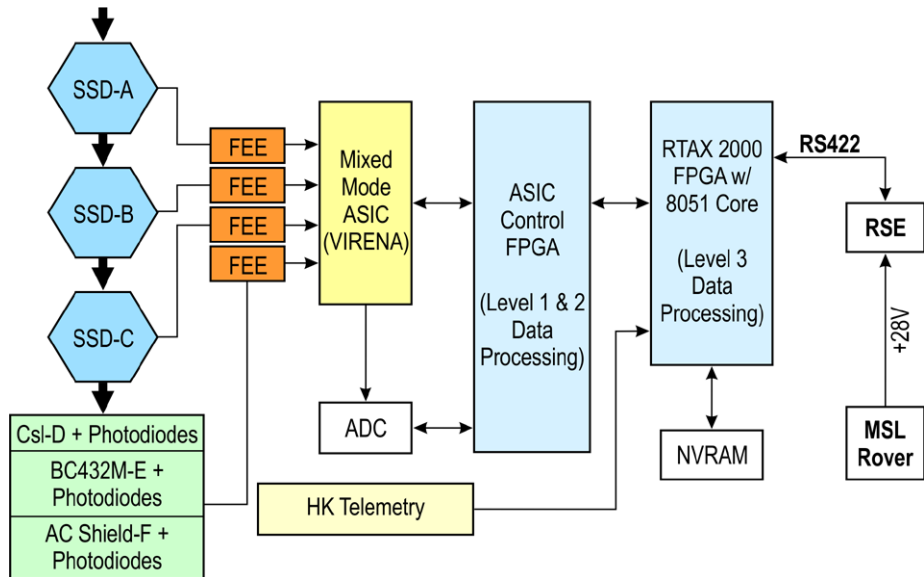


Fig. 11 Block diagram of the RAD Electronics Box (REB)

For D, the medium- and high-gain preamplifiers both have feedback capacitors of 1 pF, the low-gain preamplifier has an 8.2 pF feedback capacitor. The preamplifier outputs are connected to shaping amplifiers that are, for space reasons, located on the F2 board. The shaping amplifiers also have varying gains, $\times 1$ for the low- and medium-gain channels, and $\times 8$ for the high-gain channel. The wide dynamic range and excellent noise performance allow RAD to detect energy depositions in D as small as 1 MeV and as large as about 15 GeV. Because the light yield of the E detector (plastic scintillator) is quite low compared to that of the CsI(Tl) crystal, the feedback capacitors for those diode readouts are in all cases 1 pF so as to give relatively high gains. The shaping amplifiers have gains of 1 (low-gain channel), 4 (medium-gain), and 16 (high-gain). Like the A, B, and C channels, the D and E signals are also split and further amplified in the VIRENA.

The F1 detector is read out by three segments of the C photodiode, as described above. Each segment is connected to its own preamplifier with a feedback capacitor of 1 pF. Outputs from the three preamplifiers are ganged at the input of a single shaping amplifier with a gain of $\times 16$. Similarly, each of the three F2 readout diodes is connected to a preamplifier with a 1 pF feedback capacitor, and again outputs from the preamplifiers are ganged at the input of a single shaping amplifier with a gain of $\times 16$.

3.2 The RAD Electronics Box (REB)

The RAD Electronics Box (REB) contains three circuit boards: the RAD Analog Electronics Board (RAE), the RAD Digital Electronics Board (RDE), and the RAD Sleep Electronics Board (RSE). The functions of the boards are described in detail below. In addition to containing the sleep circuitry, the RSE board also contains all of RAD's power supply circuitry. A block diagram of the REB is shown in Fig. 11.

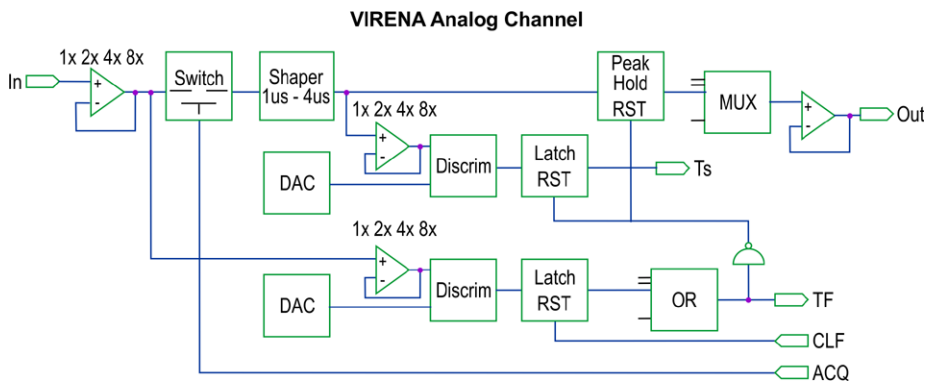


Fig. 12 Block diagram of VIRENA ASIC logic for single channel

3.2.1 RAD Analog Electronics (RAE): VIRENA ASIC, EVIL FPGA, and Digitizer

The RAE board receives the seventeen analog signals generated by the RSH. All of these are split into two channels of the VIRENA ASIC, using 34 of the device’s 36 available channels. The VIRENA (Voltage-Input Readout Electronics for Nuclear Applications, built by Nova R&D) is a mixed-signal ASIC that, for each input channel, provides amplification, two levels of discrimination (fast and slow), and two flip-flops, as described in more detail below. The VIRENA has a single multiplexed output for the analog signals, which is connected to a Maxwell 7872 14-bit analog-to-digital converter (ADC) that also resides on the RAE board.

Figure 12 is a schematic representation of the VIRENA functions for a single input channel. Each input signal is amplified by a linear amplifier stage. The available amplification values are 1, 2, 4, and 8; this is referred to as the “input gain” for the channel. The output of the linear amplifier is split into two branches. One branch goes to a shaping amplifier with selectable shaping time in the range 1 to 4 μ s. The shaping amplifier has two outputs, one of which goes to a sample-and-hold circuit (and subsequently to the ADC), the other to a second linear amplifier (also with gains of 1, 2, 4, and 8). The output of the second linear amplifier is input to a comparator; the second input to the comparator comes from an eight-bit DAC set via the FPGA. This is the “Slow Trigger” branch. When the signal exceeds the DAC voltage, the flip-flop is latched.

A second branch from the first linear amplifier goes to yet another linear amplifier (gains of 1, 2, 4, and 8). This branch is referred to as the “Fast Trigger.” The output of this amplifier goes to another comparator. The other input to the comparator comes from the “Fast DAC” for the channel. The “fast” and “slow” nomenclature refers to the relative timing of the two pulses, with the slow signal delayed by shaping.

For each input into the VIRENA, six parameters must be specified (shaping time, three amplifier gains, and two DAC settings), and there are three outputs, one analog from the sample-and-hold circuit and two logic outputs. Given that 34 channels are used by RAD, there are 204 VIRENA parameters to be configured. The individual bits that determine whether a specific fast or slow trigger fired on a given event are referred to as “tokens.”

Analog outputs from the VIRENA follow a specific naming scheme. As described above, the A1, A2, B, and C detector signals are each amplified by two independent shapers in the RSH. Each of the two outputs is further split and amplified in the VIRENA, so that there are four channels for each of these detectors. For A1, A2, and B, the nominal configuration is as shown in Table 4. For each detector, there are VIRENA outputs for low gain (L), medium

Table 4 List of RAD detector channels and nominal gains

Channel label	Feedback capacitor (pF)	FEE shaper gain	VIRENA input gain	Overall electronic gain (V per pC into preamp)
A1L, A2L, BL	8.2	×1	×1	×0.12
A1M, A2M, BM	8.2	×1	×8	×1
A1H, A2H, BH	8.2	×16	×1	×2
A1U, A2U, BU	8.2	×16	×8	×16
CL	3.3	×1	×1	×0.3
CM	3.3	×1	×4	×1.2
CH	3.3	×8	×1	×2.4
CU	3.3	×8	×8	×19
C2L	1	×8	×1	×8
C2H	1	×8	×8	×64
DL	8.2	×1	×1	×0.12
DN	8.2	×1	×8	×1
DM	1	×1	×1	×1
DI	1	×1	×8	×8
DH	1	×8	×1	×8
DU	1	×8	×8	×64
EL	1	×1	×1	×1
EN	1	×1	×8	×8
EM	1	×4	×1	×4
EI	1	×4	×4	×16
EH, F1L, F2L	1	×16	×1	×16
EU, F1H, F2H	1	×16	×8	×128

gain (M), high gain (H), and ultra-high gain (U). There is a factor of 128 in gain between the U and L channels for these detectors. For D and E, there are six VIRENA channels. From lowest gain to highest, the channels are labeled L, N, M, I, H, U. The six channels are three redundant pairs: L and N, M and I, H and U. In each case the two channels in a pair are configured to have different input gains in the VIRENA. The lower-gain channel of a given pair (L, M, H) is configured to ×1 input gain and the higher-gain channel of the pair has input gain greater than 1.

The fast trigger outputs from the VIRENA are the “Level 1” triggers for RAD. The triggering scheme is described in more detail below. Fast triggers for individual channels can be enabled or disabled, as can the corresponding slow trigger outputs. Only the fast triggers that are enabled (a small subset, nominally including only the BU, DH, and EH channels) are inspected by Level 1.

When one or more fast triggers fire, the “Level 2” trigger processing is initiated, which looks for specific (configurable) combinations of slow triggers. Up to 16 coincidence conditions can be defined in Level 2. Table 5 shows the nominal L2 trigger definitions. Ten triggers are defined; another six L2 triggers not shown in the table are used for counting purposes only, and do not initiate event readouts. If the slow token pattern matches one or more of these trigger definitions, digitization of the event proceeds according to a trigger-specific channel readout mask. Events are assigned a “hardware priority” by Level 2 which affects downstream processing. As mentioned above, only three fast triggers are enabled: BU, DH,

Table 5 Level 2 trigger definitions

Trigger type	L2 trig. #	Hits required	Channels not hit	Comments
Charged particles, outer FOV	0	A1U, BU	C2H	Low LET
Charged particles, inner FOV	1	A2U, BU	C2H	Low LET
Charged particles, outer FOV	2	A1M, BM	–	High LET, high priority
Charged particles, inner FOV	3	A2M, BM	–	High LET, high priority
B dosimetry	4	BH	–	Any ΔE in B
E dosimetry	5	EH, EI	–	Any ΔE in E
E neutral	6	EH, EI	B, C, C2, F1, F2	Neutral particle with a/c veto
D neutral	7	DH, DI	B, C, C2, F1, F2	Neutral particle with a/c veto
D-E coincidence	8	EH, EI, DH, DI	B, C, C2, F1, F2	Neutral particle with a/c veto, high priority
D heavy ion	9	DN, DM		ΔE in D with high threshold

and EH. The BU fast trigger enables the Level 2 triggers for charged particles and silicon dosimetry (numbers 0 through 4 in Table 5), while the DH and EH fast triggers enable neutral particle detection and E dosimetry (numbers 5 through 8 in Table 5).

The VIRENA control signals and parameters are provided by the EVIL (Electronics for VIRENA Logic) FPGA. The EVIL FPGA, an Actel RTAX2000S, communicates with the MSL Rover Compute Element (RCE) through the RDE board described below. The control signals and parameters are configured via a table upload. The EVIL FPGA also runs RAD's Level 1 and Level 2 firmware. This firmware controls the triggering and readout of the instrument and performs some data analysis functions. These include applying calibration factors, and determination of the most probable value of energy deposited in each detector, using the individual channels in configurable combinations. Level 1 and Level 2 triggers are highly configurable, through the same uploaded table that contains the VIRENA control parameters.

3.2.2 RAD Digital Electronics (RDE)

The RAD Digital Electronics board contains a second Actel FPGA that communicates with the RCE, the EVIL FPGA, and the data pipe. Once the analog signals that are output from the VIRENA have been digitized, they are analyzed by the Level 2 firmware, described below (Sect. 3.2.4). Real-time data analysis takes place in a virtual 8051 microprocessor instantiated in the RDE FPGA. The firmware performing this real-time analysis is referred to as Level 3, or L3.

Particle event data are sent from L2 to L3 through a FIFO buffer, with space in the FIFO buffer reserved for events marked as having high hardware priority, based on the L2 trigger. The goal is to retain as many rare events (in particular, heavy ions) as possible, even under high-rate conditions. Each event packet sent from L2 to L3 contains fields for the VIRENA fast and slow tokens, L2 trigger bits, calibrated 24-bit energy values for each channel, a “detector energy” based on combining multiple channels from each detector, and the ADC values in a compressed 8-bit format.

Level 3 maintains a 4-bit timestamp that divides the observation period into 16 segments. As mentioned above, the L2 trigger assigns a hardware priority value (0 or 1) to each event.

A different fraction of high and low priority events are digitized owing to the limited space in the FIFO. Each L3 histogram must therefore be maintained in two copies, one for high and one for low priority events. The L3 processor can efficiently calculate the approximate base-2 logarithm of a deposited energy value. This function is referred to as “RDE_log2” and is approximately equal to $8 \log_2(\Delta E)$. This compresses 24-bit ΔE values (determined in L2 using the calibration parameters) into an unsigned 8-bit result. These L2 values are used for most arithmetic, cuts, and histogram indices.

The L3 firmware populates histograms based on the energy reading digitized by the ADC and processed by L2. There are four categories of histograms: stopping charged particles, penetrating charged particles, neutral particles, and dosimetry. Each category has several associated histograms, and all valid events will populate one histogram or another. For each valid event, a “PHA priority” is assigned based on where it lands in the appropriate histogram for the event type. These values range from 0 to 3 and correspond to four PHA storage buffers. As with the hardware priority bit, the goal is to store as many relatively rare events as possible. Given the small geometry factor and relatively low fluxes of heavy ions, we expect to store PHA records for all such events. The compressed (8-bit) ADC readings, 4-bit timestamp, PHA priority, slow token mask, and readout mask make up a PHA record. The record of a given event is saved into the PHA buffer for that priority, provided the buffer is not full. Counts are kept of events stored in each buffer and the number that could not be stored because the buffer was full.

At the end of an acquisition period, the histograms, PHA buffers, counter data, and housekeeping records are packaged into a 16384-byte observation packet and stored in non-volatile memory (NVRAM) until the rover retrieves them.

3.2.3 RAD Sleep Electronics (RSE)

As mentioned in Sect. 1, rover energy constraints limit RAD to a duty cycle of less than 100 %. RAD has therefore been designed to take observations in a regular wake/sleep cadence that is handled autonomously, i.e., without commanding from the RCE. This function is implemented in the RSE board. The board also converts and conditions the 28 V power provided by the spacecraft to the lower voltages (+5 V, ± 7 V, +12 V, and -70 V) required by the RSH and other boards in the REB,

Sleep and wake durations are sent to RAD via commands from the RCE. The sleep circuit remains powered on at all times, drawing a small current of about 2 mA. While RAD is sleeping, the RSE monitors the RAD command receive line for activity (commands from the RCE, or possibly noise on the line). RAD will wake from sleep either when the internal sleep timer expires, or when the RCE sends a command to RAD. On waking, the RSE applies power to the rest of the instrument, and RAD begins the boot process. The RSE provides information to the software through the FPGA registers indicating if it was an early wake-up (command received from the RCE) or a scheduled wake-up (sleep timer expired). The software uses this information to decide if RAD should begin an observation, remain in checkout awaiting commands, or go back to sleep. The latter occurs when activity is detected on the command receive line, but no subsequent command is received within 60 seconds. It is assumed in this case that the activity detected on the command receive line was due to random noise, and RAD returns to sleep mode with no change to the sleep duration.

RAD can be configured to acquire data from 64 to 7200 seconds with 16 second resolution, and the sleep time can be independently configured from 0 to 122880 seconds with ~ 30 second resolution. Corresponding average power consumption is in the range from 4.2 W to near zero. Sleep and wake durations may be updated by command from the RCE.

3.2.4 Event Processing

RAD event processing proceeds in the following stages:

- Events are started by the VIRENA Fast Trigger (TF) signal.
- The EVIL waits for a signal integration time, then starts the Token read process.
- The VIRENA Fast Token mask is read and compared to the High Energy Pattern.
- The VIRENA Slow Token is passed to Level 2.
- Level 2 generates a Readout Token based on the Slow Token.
- The EVIL sends the Readout Token back to VIRENA to select channels to be digitized.

An asserted bit in the Readout Token specifies that the corresponding VIRENA channel is to be digitized. The readout can accordingly be configured to improve the throughput of the system. For instance, a neutral particle trigger fired only by signals from the E detector can be configured so that it only causes the E and anticoincidence channels to be read out. Digitizing only a small subset of the available channels allows RAD to be ready for the next event much sooner than if all channels had been read out. The High Energy Pattern is a mask of low-gain channels that only register hits on heavy-ion events. When enabled, it causes an extra delay in the time until RAD is enabled to acquire the next event, in order to let the analog signal lines return to quiescent levels.

In Level 2, calibration constants are applied to the digitized data for each channel to convert each pulse height to a deposited energy value. A configurable energy selection scheme is then implemented in which the most appropriate combination of channels from a given detector are selected to make the best estimate of the energy deposited in that detector. For the A, B, and C detectors, the scheme is simple: the highest-gain channel with a usable (non-saturated) signal is used. For D and E, the situation is more complicated, as light is shared among the three diodes in a position-sensitive way; therefore combining energy readings from two or more diodes in many cases yields better energy resolution than would be obtained using the energy reported by a single diode. Typically we expect at least three D or E channels to give on-scale energy readings for any given event; the deposited energy ΔE is then calculated according to $\Delta E = 0.25 (\Delta E_{\text{low}} + \Delta E_{\text{mid}}) + 0.5 \Delta E_{\text{high}}$ where the subscripts refer to the relative gains of the three channels. In some cases, only two channels may have usable signals, in which case the deposited energy is taken to be the simple average of the two energy readings.

4 Observations and Autonomous Operations

4.1 Operations Overview

RAD was initially designed to operate continuously on the surface of Mars with data being stored to internal memory every hour. However, due to energy constraints of the MSL rover power system which became apparent during the early design phase of the project, RAD was subsequently designed to operate autonomously (without commanding) for arbitrarily long observing periods, alternating with periods of a low power sleep state. This approach maintains the one hour observing cadence necessary to meet the science objective of characterizing the onset of SEP events, while reducing the overall energy requirements on the rover. This autonomous operation also enables RAD to continue to operate even when the Rover Compute Element (RCE) is asleep. RAD's wake/sleep cycle is described in Sect. 3.2.3.

While awake, RAD collects, bins, and formats its measurements, and saves the data to NVRAM. The data remain in NVRAM until the RCE is ready to transfer them to the Rover

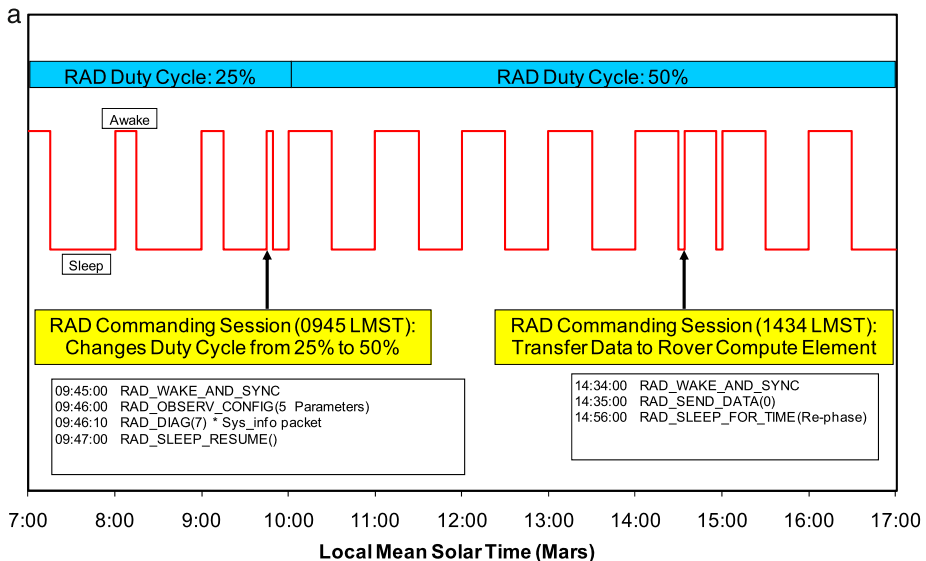


Fig. 13 (a) A “day in the life” of RAD on the surface of Mars, from the perspective of interaction with the rover. (b) RAD state transition diagram

for subsequent downlink to Earth. Once the wake and sleep durations are set, RAD continuously cycles through them until commanded otherwise. Figure 13(a) illustrates a “day-in-the-life” for RAD where a change is made to the observation duty cycle in the morning and science data is transmitted from RAD to the RCE in the afternoon. Changes to the observation duty cycle may be infrequent, in which case the only interaction with the RCE is the data transfer or RAD_GetData activity.

4.2 Commanding Philosophy

RAD is designed for simple and minimal commanding throughout the mission. For most of the mission, RAD only requires daily data transfer sessions. Of course, instrument operational parameters can be changed as necessary via command. Note that all commands and sequences will first be validated on the ground, both standalone and as part of a Sol’s activities.

When power is applied to RAD, the instrument enters the BOOTUP state and performs various initialization tasks. A “boot wait time” parameter is used to allow RAD to complete initialization after power-up. The boot wait time parameter is set to 30 seconds. When initialization is complete, RAD will automatically transition to the SCIENCE state. If no command is received within 60 seconds after power-up, RAD will go to sleep and will enter the sleep/observe cycle in its default configuration table. Due to the largely autonomous nature of RAD operations it is expected that the RCE power switch for RAD will not normally be cycled. Duty-cycling of RAD operations will be performed through the RAD-controlled sleep/wake cycle (which effectively applies and removes power from the main instrument electronics).

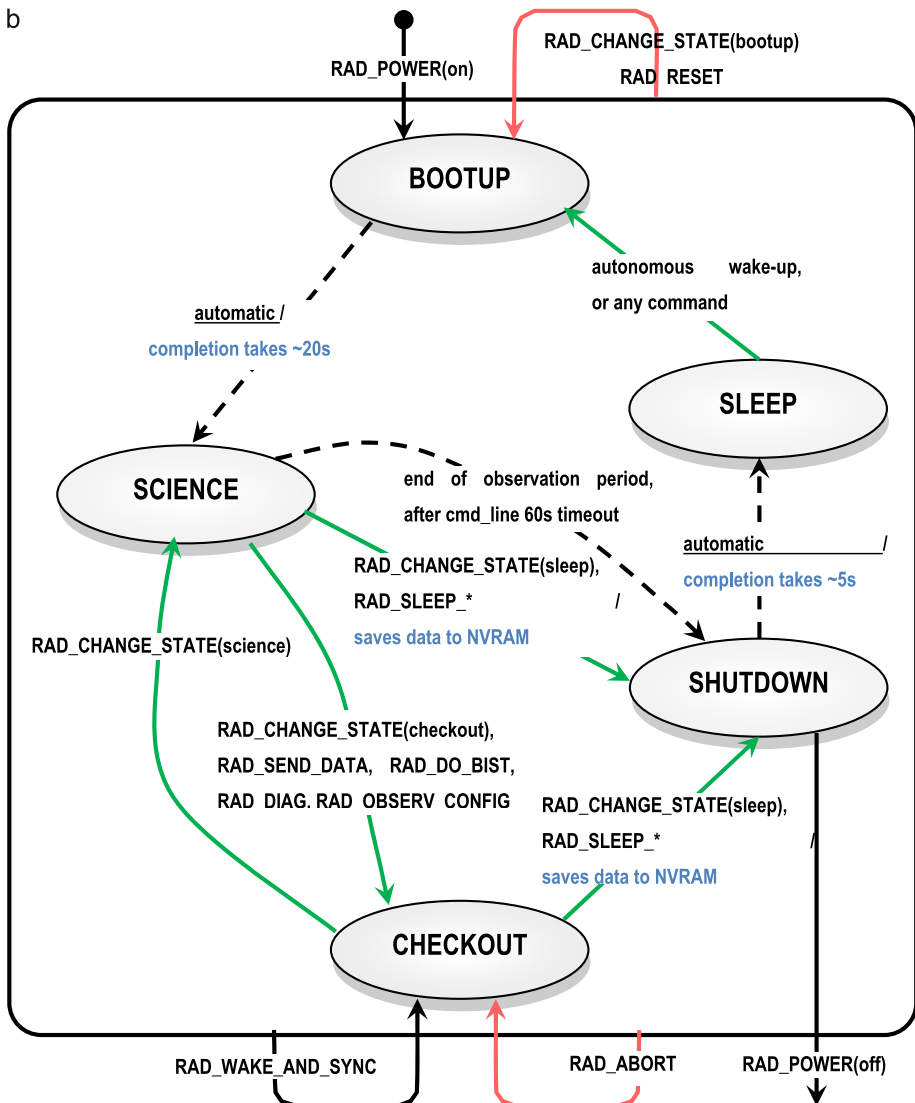


Fig. 13 (Continued)

4.3 Operating States and Transitions

From the point of view of the spacecraft command interface, RAD can be OFF or in one of four distinct states described in Table 6 and illustrated schematically in Fig. 13(b).

During normal operations, RAD collects data by waking up from SLEEP, performing autonomous observations in the SCIENCE state, saving data in RAD Non-Volatile Memory in SHUTDOWN state, and then going back to SLEEP. The CHECKOUT state can be entered from the SCIENCE state and is used to perform data transfer to the RCE, and maintenance and troubleshooting activities.

Table 6 Instrument states

State	Description	RCE state	Commanding	Data produced
OFF	Power to the RAD is off	n/a	None	None
BOOTUP	Checks PROM and EEPROM integrity, configures RSH for expected environment, transitions to SCIENCE state	On or Off	None	None
SCIENCE	Science data is collected	On or Off	All commands except memory commands	Science data, housekeeping, messages
CHECKOUT	Can perform memory loads, dumps, RAM checkout, self-diagnostics and data transfer to RCE	On	All commands	Engineering, housekeeping, messages
SHUTDOWN	Processes and stores science data in NVRAM, saves internal parameters for next observation, loads sleep timer and initiates sleep state	On or Off	None	None
SLEEP	Main 28VDC supply is on, RAD secondary supplies are off. RDE is not powered. RAD monitors Rx line for activity, or waits prescribed sleep duration to complete	On or Off	Any toggle on the command line wakes RAD	None

4.3.1 SLEEP Mode

In the SLEEP state, the instrument only draws power for a timer circuit (~ 100 mW) within the RAD Sleep Electronics, on the primary side of the DC/DC converter. The sleep and wake behavior is described in more detail in Sect. 3.2.3.

4.3.2 SOLAR_EVENT Mode

A SOLAR_EVENT flag is extracted by the Wake-up Monitor when there is an indication by RAD that a high particle flux is being detected during the “pre-observation” measurements, which are taken for approximately 10 seconds during the BOOTUP process before the regular SCIENCE observations begin. The SOLAR_EVENT flag can only be set during this “precursor” observation. The flag is NOT set if high event rates are encountered during nominal science observations. The flag persists until the science data packets containing the observation made in SOLAR_EVENT mode are read out of RAD to the RCE. RAD marks science-data packets collected under the SOLAR_EVENT condition as HIGH_PRIORITY_DATA. This flag may be useful for MSL operations, as it can serve as a warning for potentially threatening radiation conditions (i.e., large SEP events).

4.4 Data Transfer

Data transfer from the instrument to the RCE is accomplished by sending a “RAD_SEND_DATA()” command, which iteratively invokes the “SEND_DATA” command. This must be done with RAD in the CHECKOUT state. The SEND_DATA command is automatically iterated by the RCE. Multiple science data packets (16384 bytes) are transferred, each forming individual RAD_Send_Data data products, until the RCE gets an indication that there are no more science data packets to transfer from RAD.

Fig. 14 Photo of the RAD Flight Model (FM) prior to integration with the MSL rover



Transfers will occur roughly once per sol, so typical data volumes will be \sim 400 kBytes per session. However, RAD has 16 Mbytes of NVRAM for data storage, which is enough to hold several tens of days of observations at a rate of one observation per hour. Some science packets may be marked as high-priority. These packets contain especially interesting data (i.e. Solar Event or critical messages) and are given higher downlink priority than standard RAD science data products.

4.5 Flight SW Versions

The instrument stores four copies/versions of its software internally: three in EEPROM and one in PROM. Each EEPROM image can be different. When RAD enters BOOTUP, it checks the EEPROM image designated by a parameter stored in NVRAM. If the image is valid, it is loaded into RAM for execution. If the selected version is not valid, RAD tests the next image. If none of the EEPROM images are valid it will load the PROM version.

5 Model Philosophy and Calibration

Two Flight Model (FM) RAD Sensor Heads were built, along with one flight-ready RAD Electronics Box. A photograph of the Flight Model RAD is shown in Fig. 14. The FM RSH's

Table 7 RAD calibration campaigns

Facility	Description	Date(s)
Charged particles		
SwRI	^{207}Bi source (e^- lines at 482 and 976 keV), sea-level muons	Monthly, pre-delivery
NSRL (BNL)	Protons, carbon, iron	2007
HIMAC (Japan)	Protons, helium, carbon, silicon, iron with CalRAD in flight-like configuration	2009, 2010, 2011, 2012
Neutrons		
PTB (Germany)	Quasi-monoenergetic neutrons, 5, 15, 19 MeV	2010, 2011
NIRS (Japan)	Calibrated AmBe source	2009, 2010, 2012
iThemba (S. Africa)	Quasi-monoenergetic neutrons, 60, 100 MeV	2008, 2011
TSL (Sweden)	Quasi-monoenergetic neutrons, 22, 46, 75 MeV	2012

are referred to as FM1 and FM2. The FM2 RSH was chosen for flight, and the FM1 RSH was mated to an Engineering Model REB to be as close to flight-like as possible. This combination is referred to as CalRAD, and the unit has been used for several calibration runs at beam facilities. Its performance is nearly identical to that of the full FM unit, based on test results obtained with both sensor heads in ion beams at the NASA Space Radiation Laboratory (NSRL). Both FM RSH's and the FM REB were individually subjected to vibration and thermal-vacuum testing. The mated FM unit was also subjected to the same tests. All units passed all environmental tests.

5.1 Calibration Overview

RAD has undergone extensive calibration campaigns to fully characterize its response to both charged and neutral particles. A list of calibration facilities used to calibrate RAD is listed in Table 7. The main purpose of calibration is to determine, for each channel, the relation between the pulse height as reported by the 14-bit ADC and the deposited energy. Calibration constants are applied to ADC values in Level 2; this is required for the onboard histogramming to work properly. Since a large fraction of RAD data are histogrammed and not stored as full PHA records, it is essential that calibration (and hence the histograms) be accurate. In the case of the silicon detector readout channels, there is a simple, highly linear relationship between ΔE and pulse height, and the gain is calculable from first principles given knowledge of component values (see Table 5). Calibration is still needed, since offsets vary from channel to channel, and there are normal, small variations from nominal in the component values. Small parasitic capacitances can also contribute, particularly for the channels with the highest gain (lowest feedback capacitor values). The situation is more complicated for scintillators, as described in the following.

Given the importance of calibration for RAD, and the considerable effort that the team has made in this area, the remainder of this section should be considered merely an overview. A manuscript with more detailed information is currently in preparation.

5.1.1 Quenching of Scintillator Light Output

For scintillators, it has long been known (Birks 1964) that there is a non-linear relationship between ΔE and light output due to quenching. Birks' empirical formula is given by:

$$\frac{dL}{dx} = \eta \frac{dE/dx}{[1 + k_B(dE/dx)]}$$

where η is a constant, dL/dx is the light output per unit path length, dE/dx is the ionization energy loss, and k_B is empirically determined. In principle k_B is a function of the charge and mass of the ion being measured. It will be different for plastic scintillator than for CsI(Tl). (Quenching is a larger effect in organic scintillators.) The situation is further complicated for RAD by the non-trivial geometry of some of the scintillators—D and F1 especially—and the *a priori* unknown light collection efficiencies. Complete calibration of scintillators requires a mapping over many ion species and energies to determine the dependence (if any) of the k_B values (determined separately for D and E) on these variables. As can be seen in Table 7, many combinations have been measured. Analysis of PTB neutron data shows that assuming k_B is a constant for each scintillator ($6 \times 10^{-3} \text{ MeV}^{-1} \text{ g cm}^{-2}$ for E, $6.8 \times 10^{-4} \text{ MeV}^{-1} \text{ g cm}^{-2}$ for D) is sufficient to correct spectra recorded from 14.8 and 19 MeV neutrons (Kortmann 2010; Köhler et al. 2011). The value of k_B for E is smaller than the value of $1.3 \times 10^{-2} \text{ MeV}^{-1} \text{ g cm}^{-2}$ found in the literature for the similar material NE-102 (Craun and Smith 1970).

Quenching corrections introduce complexity into the calibration that are beyond the capability of the on-board processing hardware to handle. The scintillator channels are therefore calibrated using muon data collected in overnight runs, and 1 GeV proton data obtained at NSRL. Both are sparsely-ionizing particles for which quenching is minimal. The energy scales can be thought as “muon equivalent.” As a result, the stopping and penetrating particle histograms that are part of the observation packet (and part of the Reduced Data Records, or RDRs, that will be made publicly available) are populated in different bins than would be the case without quenching. This will be handled by providing a map that in essence translates from a particular bin of the stopping histogram to a most probable charge and energy range. In the penetrating particle histograms, a mapping will be provided to most probable charge. More sophisticated (and likely more accurate) analysis will be possible using the PHA event records that will be telemetered to Earth. The histograms and their associated mappings are described in more detail in Sect. 7.

5.1.2 Streaming-Mode Data

By design, RAD produces highly compressed science data in the form of “observation packets,” described in Sect. 7. The compression accommodates the small telemetry allocation, but in ground-based testing this constraint does not exist. To facilitate the calibration of the instrument and our understanding of its behavior, a “streaming mode” of data acquisition was implemented. This required modification of the firmware that runs in RAD as well as implementation in Ground Support Electronics (GSE). In streaming mode, the full, uncompressed event packet produced by the onboard Level 2 firmware is output via RAD’s RS-422 connector. This mode is not implemented in the flight unit. In RAD’s normal operating mode, event packets are processed on board by the Level 3 software, which produces histograms and saves a fraction of event records in a highly compressed format. The full packet contains detailed information about the event including bitmasks for the fast tokens, slow tokens, Level 2 triggers, and readout channels; a timestamp; and raw, uncompressed ADC values for all channels that were read out on the event. These data allow us to determine the relationship between the known deposited energy (which in all cases must be calculated) and the ADC reading in a given channel.

5.2 Bismuth-207 Calibration, Temperature Compensation

The RAD flight unit was fully assembled, integrated, and tested in preparation for a December 2008 delivery. Prior to thermal testing, it was determined that placing a ^{207}Bi source on

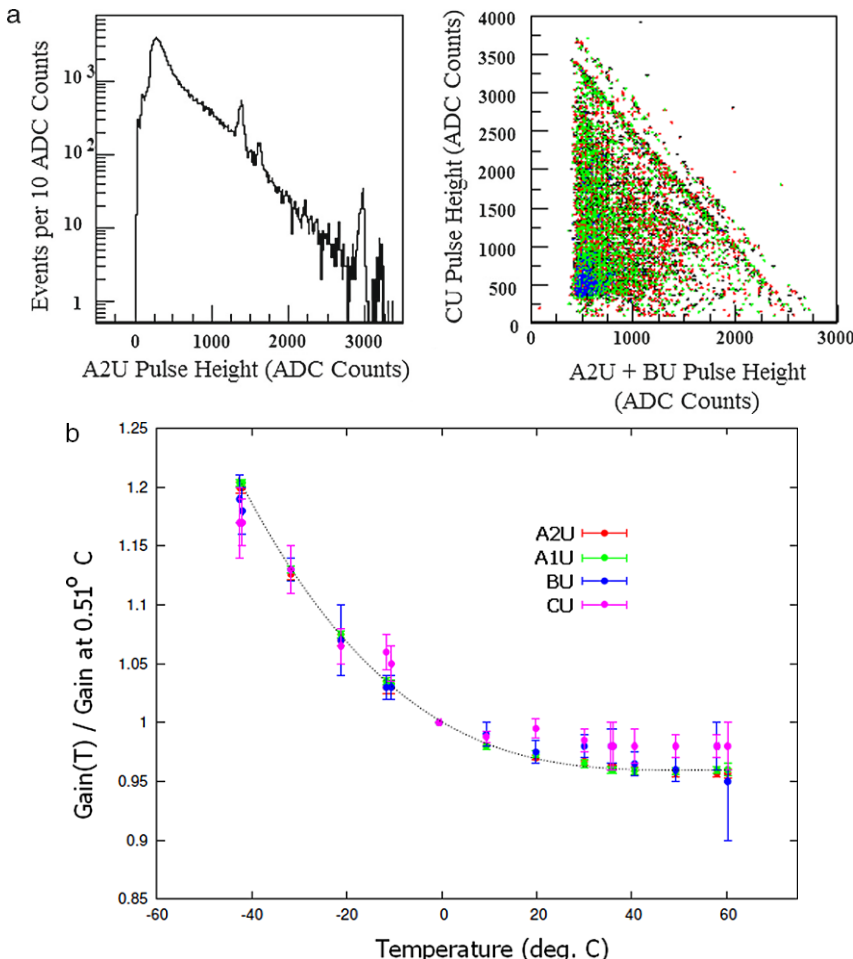


Fig. 15 (a) Calibration data taken with a ^{207}Bi source on the flight unit. The plot on the left shows the spectrum in the A2 detector, with five distinct electron lines. The scatter plot on the right shows a dense cluster of minimum-ionizing events (lower left) and bands corresponding to 975.7 and 1060 keV electrons that stop in C. (b) Temperature dependence of gains for A1, A2, B, and C ultra-high-gain channels. Other channels show the same trend

top of RAD and acquiring data was feasible. This was a crucial test since key electronic components inside RAD have unpredictable temperature dependences. The CsI and plastic scintillators also have temperature dependence in their light output (particularly the CsI). Taking source data allows us to map the changes in offset and gain for all channels as functions of temperature. The ^{207}Bi source emits significant numbers of electrons at energies up to 1060 keV, with particularly intense emission at 975.7 keV and 481.7 keV. The decay electrons with the highest energies can—if they do not undergo significant scattering—pass completely through the A, B, and C detectors, barely reaching D (and depositing a minuscule amount of energy) before stopping. Electrons that undergo large scatters can lose all their energy in a single detector; others may pass through A and stop in B, or pass through A and B and stop in C.

The various fates of electrons emitted from the ^{207}Bi source can be seen in the two plots in Fig. 15(a). The left panel shows the spectrum recorded in the A2U (highest gain readout channel for the inner segment of A), in units of ADC counts after pedestal subtraction. The large peak at about 280 ADC counts is from electrons passing straight through the A diode, depositing about 100 keV. These ~ 1 MeV electrons are minimum-ionizing. The signals are well separated from the pedestals in A, B, and C, which unambiguously demonstrates RAD's capability to measure the lowest LET's it will encounter in flight (~ 0.2 keV/ μm). Moving to the right, the next peak, around 1390 ADC counts, is from stopping 481.7 keV electrons. Their energy deposition in A2 is actually somewhat less (we estimate 443 keV) than the full energy, due to losses in the windows in between the source and the detector. The next peak (channel ~ 1610) is from stopping 553.8 keV electrons. The final strong peak is seen around channel 2960, from stopping 975.7 keV electrons that actually deposit about 941 keV. A small cluster of events, centered at channel 3190, can also be seen, due to 1060 keV electrons. In between peaks, there is a continuum of energy depositions due to scattering and other emission energies. In the right-hand plot in Fig. 15(a), we show the combined signals in A2U and BU on the y-axis, plotted against the CU signal on the x-axis. The dense cluster of events in the lower left-hand corner of the plot is due to electrons that pass (more or less) straight through all three detectors. Two parallel diagonal bands of constant total ΔE can be seen. These are populated by 975.7 and 1060 keV electrons that stop in C, with the 975.7 keV band being comparatively densely populated.

Comparable histograms of the BU and CU spectra are not as rich in detail, but nonetheless yield one or two points each that can be used to determine the temperature dependence of the gains. Note that temperature variations in pedestals can be determined for all channels using the thermal test data, but gain variations can only be mapped for A, B, and C. Since the charge yield of the silicon detectors is essentially independent of temperature, gain changes in these channels must be due to changes in the electronics. Careful analysis of the data shows that all channels that can be analyzed (U, H, and M—signals in the L channels are too small) show the same trend vs. temperature. This is shown for the U channels in Fig. 15(b). For temperatures of 10 °C and above, measured gains are consistent with being temperature-independent. Below 10 °C, gains increase as temperature decreases, reaching a relative increase of 15–20 % at -45 °C. The observed temperature dependence is expected, due to the large temperature coefficients of the polysilicon resistors integrated in the ASIC, which change the shaping time constant and thus the peak height of the shaper output.

Since all measured channels show nearly-identical behavior, we assume all channels in the system show the same trend. The D and E detectors were not hit by the ^{207}Bi electrons, so they have not been fully tested. However, we can reasonably assume the same temperature dependence for the electronics for those channels, and for D we can factor in the known temperature dependence of light yield based on the published value of -1.4 % per °C (Nakamura et al. 2010). Temperature corrections for E are negligible: according to the manufacturer, the light yield of BC-430 (very similar to the BC-432m used in RAD) is independent of temperature from -60 °C to $+20$ °C, and decreases by only about 5 % in the range $+20$ °C to $+60$ °C (~ 0.1 % per °C).

The design of the RAD firmware anticipates the need to make significant corrections to the calibration in on-board data processing. RAD's real-time histogramming depends on having accurate deposited energy measurements, which in turn depend on accurate calibration regardless of the temperature. Accordingly, eight configurable temperature compensation tables are defined, spanning the expected operating range of -20 °C to $+55$ °C. Compensation is implemented as follows: before RAD begins an observation, it takes a temperature reading, and based on that reading, selects the table that corresponds most closely

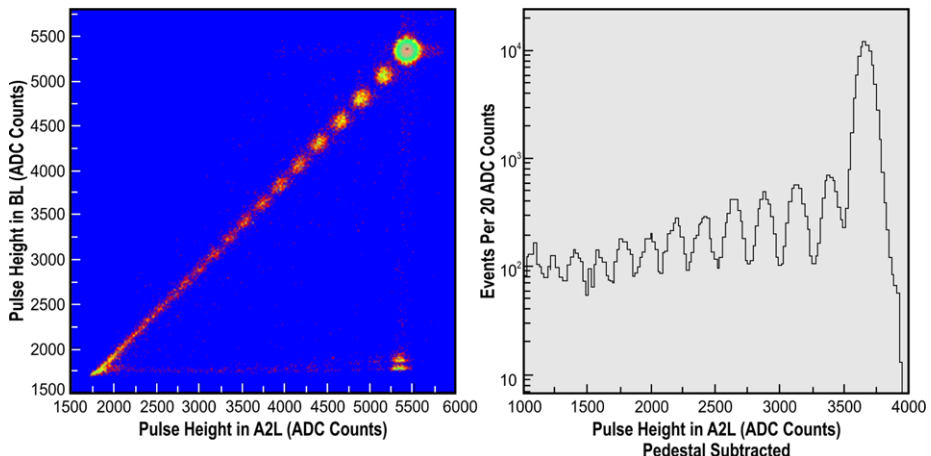


Fig. 16 RAD calibration data from NIRS showing iron and fragments after a 500 MeV/nuc beam is passed through a 4.5 g cm^{-2} polyethylene target. *Left:* Scatter plot of B detector signal vs. A2 detector signal. *Right:* Histogram of A2 pulse height. Data shown are from low-gain readout channels. These and similar data were used to determine calibration gains as explained in the text

to the measured temperature. Each compensation table provides “deltas,” that is, generally modifications to the thresholds settings, calibration offsets (pedestals), and gains from the nominal. The deltas are applied by L2 to the nominal values taken from the EVIL table.

5.3 Charged Particle Beams

5.3.1 A, B, and C Detectors

The muon and ^{207}Bi calibration data described above are most useful for RAD’s high-gain channels. Data taken with heavy charged particle beams are useful for calibration of the low gain channels, and to demonstrate that RAD meets the requirements of having a wide dynamic range (LET from 0.2 to $\sim 1000 \text{ keV}/\mu\text{m}$), and good dE/dx resolution. In a well-collimated high-energy heavy ion beam, it is possible to place a target of moderate depth in the path of the beam to produce fragments with velocities very near equal to those of the beam ions. When velocities are equal, ΔE simply scales with the square of the charge, so that fragment peaks in the spectra can be used as additional calibration points. Figure 16 shows an example of the method, using data taken with a 500 MeV/nuc ^{56}Fe beam ($Z = 26$) and a 2.9 g cm^{-2} polyethylene target. At this energy, the ^{56}Fe ions have LET of about $206 \text{ keV}/\mu\text{m}$ as they leave the target, and about 70 % of the beam ions survive traversal of the target intact. (The remainder fragment into lighter ions.) The left panel shows a scatter plot with color-coded intensity map (logarithmic sensitivity) of the pulse height in low-gain channels, BL vs. A2L. Several features are apparent:

- a densely-populated cluster of Fe events in the upper right-hand corner;
- clusters of Mn ($Z = 25$), Cr ($Z = 24$), etc., fragments along the 45° line;
- a continuum along the 45° line at lower pulse heights;
- a band along the bottom, consistent with a beam ion or fragment hitting A2 but grazing or entirely missing B (A2 is slightly larger in area than B, see Fig. 9).

Fragment clusters can be distinguished down at least as low as charge 16 in this figure. The clusters begin to merge into a continuum as charge decreases because the velocity distributions of the fragments begin to broaden, and because the ΔE from non-leading fragments begins to contribute significantly to the total.

The right-hand panel of Fig. 16 shows the pulse height histogram in A2L after pedestal subtraction. Peaks down to charge 14 are seen; the apparent worsening of resolution with decreasing charge is due to the physics effects described above and not due to any loss of resolution in the detector or in the readout. The ΔE of the iron ions in this plot is calculated to be about 120 MeV, almost exactly 1000 times larger than the ΔE for minimum-ionizing particles. The Fe peak is at channel 3640, giving a gain factor of about 30.3 ADC counts/MeV. This is in excellent agreement with a first-principles calculation of the gain of this channel, which gives 29.6 ADC counts/MeV.

In terms of LET,¹ the gain factor determined above from the iron peak is 17.67 ADC counts per (keV/ μm). The full scale ADC reading is, after pedestal subtraction, 14600 counts. Extrapolating linearly, the maximum LET that can be measured without saturation is 826 keV/ μm , which corresponds to ^{56}Fe with about 50 MeV/nuc of kinetic energy. The implications of this are discussed in Sect. 6. The gain factor obtained from the Fe peak alone can be checked by using a few of the other fragment peaks, if we assume equal velocities, a good assumption for the first few fragment species below the primary Fe. The points fall on a line (forced to have an intercept of 0) with a slope of 17.75 ADC counts per (keV/ μm).

Lighter beam ions such as carbon and silicon have been used to calibrate the gains of the medium- and high-gain channels. The same methods are applied, and the gains of those channels are also found to agree with the expected gains to within a few percent.

5.3.2 D and E Detectors

Full calibration of the D and E detectors is challenging due to quenching. As noted above, light output is approximated by Birks' formula, and while values for k_B have been found for D and E in neutral-particle data (where the signals are generated by low-energy recoil protons), those values are not necessarily applicable to the responses of the detectors to high-energy ions. As an example, we show in the left panel of Fig. 17 a scatter plot of pulse height in the EN channel vs. pulse height in the A2M channel for a beam of 800 MeV/nuc ^{28}Si ions ($Z = 14$) and a 4.5 g cm^{-2} polyethylene target. The response of the A2M channel is linear in ΔE , but the response of E is not, due to quenching. Clusters of events are seen down to about charge 8, mainly due to the good resolution in A2M. Each cluster has a tail to low pulse height in EN; these are populated by events in which the ion fragments after passing through A2, most likely in D or E.

The effect of quenching can be demonstrated by looking at the same readout channel, EN, for different beams, as shown in the right panel of Fig. 17. Points for a 180 MeV proton beam, a 160 MeV/nuc ^4He beam, and the aforementioned ^{28}Si beam are plotted. For each point, the calculated ΔE is on the x -axis, and the center of the measured pulse height distribution (after pedestal subtraction) is on the y -axis. The solid line was obtained by fitting a line to the proton and helium data points; the silicon-beam point falls far below the extrapolated line, with a pulse height about 2/3 as large as would be expected without

¹Scaling to LET assumes a constant ratio between dE/dx in silicon and dE/dx in water. This is a good approximation at high energies, but it becomes less accurate below about 200 MeV/nuc.

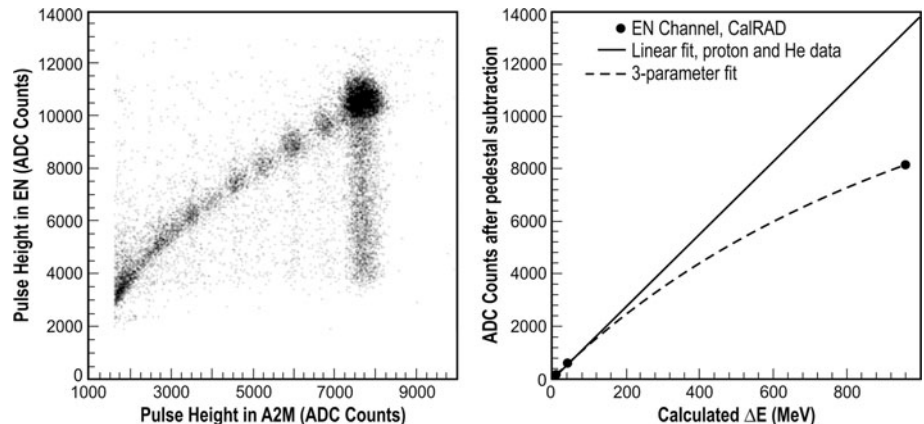


Fig. 17 *Left panel:* Calibration data from HIMAC with an 800 MeV/nuc ^{28}Si beam incident on a 4.5 g cm^{-2} polyethylene target. Pulse height in the EN channel (readout of the plastic scintillator) is plotted against the medium-gain readout of the A2 silicon detector. *Right panel:* Peak ADC values for the EN channel for three different beam ions, showing the effect of quenching. Data from NIRS

quenching. A three-parameter fit is also shown, using a form meant to be suggestive of Birks' formula:

$$\text{PulseHeight} = \text{offset} + \frac{\text{gain} \cdot (\Delta E / \Delta x)}{1 + k \cdot (\Delta E / \Delta x)}$$

With three points and three free parameters, the fit is constrained to pass through all the data points. The value of k is found to be $1.3 \times 10^{-3} \text{ cm MeV}^{-1}$, a factor of 5 less than the k_B value found for recoil protons (see Sect. 5.1.1 above), and a factor of 10 less than the k_B value found in the literature. This preliminary result may seem surprising at first glance, but one should bear in mind that dependence of k_B on ion species and energy is expected. Further, the functional form used in the fit may not yield a k value that is directly comparable to k_B because we have integrated over dE/dx in a single step.

As mentioned above, conversion of pulse height to ΔE in real time by the Level 2 firmware cannot accommodate the complexity introduced by quenching corrections. The onboard calibration parameters for the D and E channels are therefore obtained from low-LET particles (proton and helium beams, and muons). The quenching corrections, which are still being studied, will be applied in ground analysis. The RDR science data will include a map from our onboard histograms to charge and energy with quenching taken into account.

5.4 Neutron Beams and Inversion Method

Considerable effort has been devoted to gaining a detailed, quantitative understanding of RAD's response to neutral particles (Kortmann 2010; Köhler et al. 2011). A full description of the methods can be found in these references, and repetition of the details is beyond the scope of this work. However, a brief overview is given for completeness.

The general problem of unfolding a neutron spectrum is well known and has been studied for decades (Burrus and Verbinski 1969, and references therein). When used as neutron detectors, plastic scintillators typically record partial energy deposits caused by recoiling carbon or hydrogen nuclei. The full energy is typically not deposited in the detector, and even if all the energy of the incident neutron is transferred to recoil protons (the best case),

there are typically many such protons sharing the energy unequally. Light output from such low-energy protons is heavily quenched. Thus even if one could somehow select an event sample containing only those events where the full neutron energy was transferred to recoil protons, the resulting light output distribution would be broad. The usual situation is that light output spectra in this situation are nearly flat, and featureless. The measured pulse-height spectrum, assumed to be binned, can be related to the true spectrum as follows:

$$\begin{pmatrix} M_1 \\ M_2 \\ M_3 \\ \vdots \end{pmatrix} = \begin{pmatrix} r_{11} & r_{12} & r_{13} & \dots \\ r_{21} & r_{22} & r_{23} & \dots \\ r_{31} & r_{32} & r_{33} & \dots \\ \vdots & \vdots & \vdots & \ddots \end{pmatrix} \begin{pmatrix} T_1 \\ T_2 \\ T_3 \\ \vdots \end{pmatrix}$$

where M_i refers to the number of events measured to be in pulse-height bin i , T_j refers the actual number of neutrons in energy bin j , and the r_{ij} define the detector response function. The response function matrix is usually determined by a combination of calibration data and Monte Carlo simulation. Ideally one would hope to simply make the measurement and apply the inverse of the response function matrix in order to obtain the true neutron energy spectrum. In practice, however, this is usually not possible as the matrix often proves to be non-invertible. Further, even if the matrix can be inverted, results are extremely sensitive to statistical fluctuations in the data and tend to show strong negative bin-to-bin correlations. Such unphysical results are highly undesirable.

RAD is sensitive to both neutrons and γ -rays. Although γ -rays are not expected to contribute significantly to the dose on the surface of Mars, their flux may be considerable, and we have no *a priori* way of distinguishing their energy depositions from those of neutrons. The D detector is more sensitive to γ 's than is E, but E has some sensitivity, and both are sensitive to neutrons, with approximately equal interaction probabilities in the neutron energy range of interest. The joint inversion can be thought of in terms of a slightly different set of matrices:

$$\begin{pmatrix} M_D \\ M_E \end{pmatrix} = \begin{pmatrix} r_{D\gamma} & r_{Dn} \\ r_{E\gamma} & r_{En} \end{pmatrix} \begin{pmatrix} T_\gamma \\ T_n \end{pmatrix}$$

where we now relate measured spectra in D and E (represented by M_D and M_E , which are vectors) to the true γ -ray and neutron spectra T_γ and T_n via the submatrices $r_{D\gamma}$ (response of D to γ -rays), $r_{E\gamma}$ (response of E to γ -rays), etc.

The method to be used in ground analysis is a joint inversion based on Poisson statistics (Köhler et al. 2011). It has been developed and refined using 14.8 and 19 MeV neutron beam data obtained at PTB. The response functions, calculated with GEANT4, can be put in terms of geometry factors; these are shown in Fig. 18. As expected, for γ -rays, D has larger geometry factors (greater sensitivity) than does E; the reverse is true for neutrons. Figure 19(a) shows the measured and simulated spectra for the two beam energies, for D (plots on the left) and E (plots on the right). The good agreement gives us confidence that the response functions are being modeled accurately. Figure 19(b) shows the results of inverting the data using these response functions, and three different inversion methods, with γ -ray spectra on the left and neutron spectra on the right. RAD ground analysis will use the method labeled in the figure as “Poisson.” The 14.8 and 19 MeV beams are represented by large spikes in the neutron spectra at the correct energies using the Poisson-based inversion. As a further test, the data sets were artificially mixed together, and the inversion methods were applied. The results are shown in the bottom panels of Fig. 19(b): again, large peaks appear at the correct energies, suggesting that the method is quite robust.

Fig. 18 Matrices showing geometric factor (given by the color scale *on the right*) as a function of detected energy vs. actual particle energy for the D and E detectors

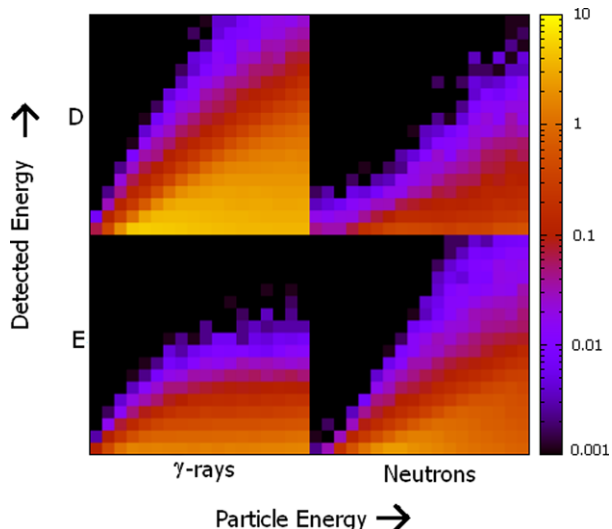


Figure 20 shows model calculations of the radiation environment on the surface of Mars (Tripathi and Nealy 2008), produced with the HZETRN model, as well as the coverage provided by RAD. To date, calibration of RAD over the energy ranges and particle types shown has been completed with the exception of the neutron channel. As discussed above, we have validated the neutron inversion method for RAD to \sim 19 MeV, covering the lower portion of RAD’s neutron range. Although much of the neutron flux of interest is at higher energies, extending the joint inversion method to these higher energies is difficult in part due to the lack of reliable physics models for neutrons with energies greater than 20 MeV. While it is still possible to use GEANT4 (or some other model) to calculate the matrix elements at higher energies, the lack of validating data means they are highly uncertain. To mitigate this situation, and extend the RAD neutron inversion technique to its full energy range, CalRAD was placed in quasi-monoenergetic neutron (QMN) beams at 22, 46, and 75 MeV at the TSL facility in Uppsala, Sweden (Prokofiev et al. 2006). The detector was placed at various angles with respect to the beam direction so the response could be determined separately for neutrons coming from the top, the side, and the bottom of RAD. Figure 21 shows scatter plots of the energy deposited in E vs. the energy deposited in D for the 46 and 80 MeV beams. CalRAD was placed so that neutrons entered E first. In this geometry, recoil protons may be knocked out of E into D. A significant γ -ray background, produced by neutrons interacting in the beam dump at the end of the transport line, can be seen in the lower left corner of each plot. Energy scales were determined with flight-like calibration parameters, i.e., with no corrections for quenching. The depth of the E detector is sufficient to fully contain a 45 MeV proton going straight through from top to bottom (or vice-versa); the E spectra cut off at this energy. The D detector can contain protons up to about 95 MeV, and with the higher-energy neutron beam, energy depositions in D are seen up to the full neutron energy. A fairly sharp diagonal line is seen in the 46 MeV data, corresponding to events in which the full energy of the incident neutron was captured by the two detectors. Further analysis of these data is in progress.

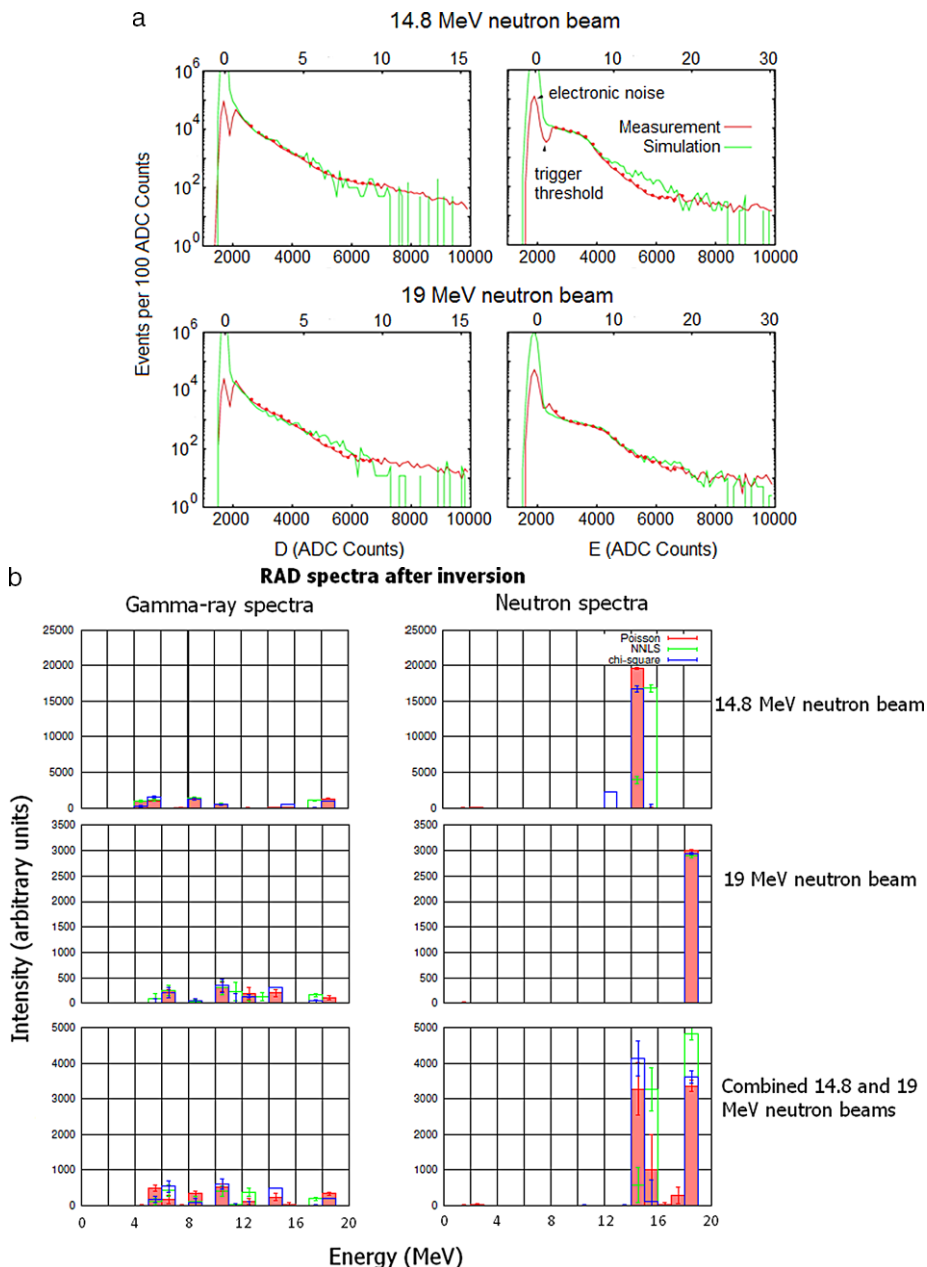


Fig. 19 (a) RAD D and E channel data obtained with neutron beams at PTB, compared to GEANT4 simulation (Köhler et al. 2011). In each plot, the upper scale is energy in MeV, the lower is pulse height in ADC counts. Agreement between the data and the simulation should not be expected in the regions below the trigger threshold. (b) PTB neutron measurements. Results are shown for three methods, one based on Poisson statistics (red), one using non-negative least squares (green), and one based on chi-squared minimization. After inversion, peaks are seen in the neutron spectra at the correct beam energies. Gamma-ray spectra are featureless and sparsely populated. As an additional test case, data from the two beams were combined and the inversion was performed; the resulting spectrum again shows peaks at the beam energies (Köhler et al. 2011)

Fig. 20 Calculated radiation environment at the surface of Mars (Tripathi and Nealy 2008), with RAD sensitivity indicated for different particle types

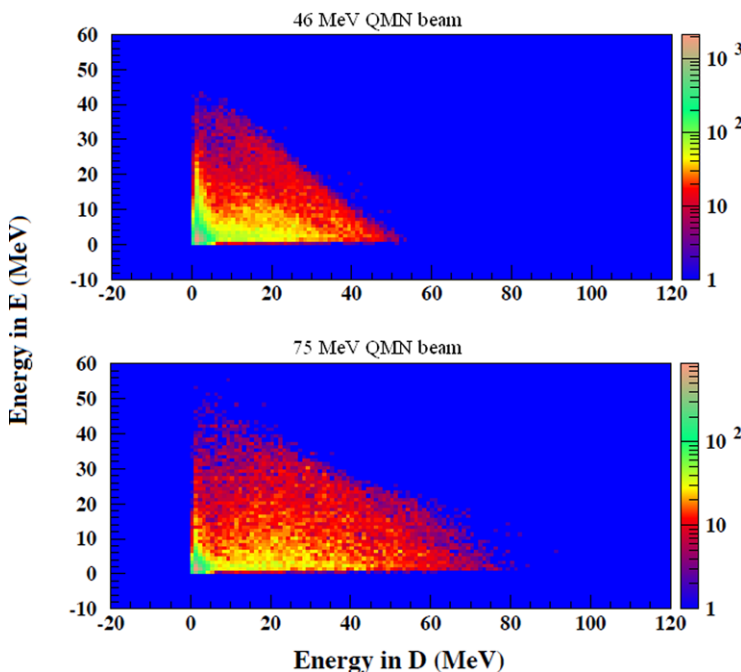
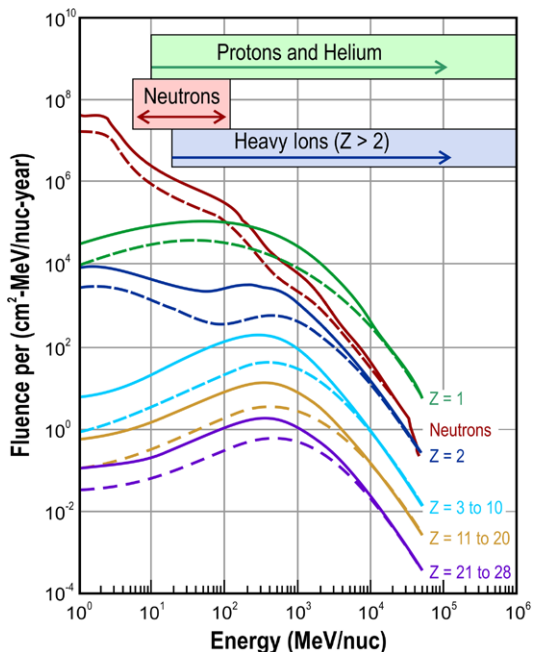


Fig. 21 Calibration data taken with CalRAD in high-energy QMN beams at TSL. Neutrons entered RAD from the bottom (i.e., the “surface” direction on Mars). Each panel shows a scatter plot of the energy deposited in the E detector against the energy deposited in the D detector. The color scale indicates the number of events per bin

Table 8 Expected statistics for GCRs

Particle type	Number acquired per 180 days	Statistical accuracy (%)	Required accuracy (%)
Primary protons	8×10^5	0.1	5
Primary helium	8×10^4	0.4	10
$Z = 5$ to 8	3×10^3	1.9	10
$Z = 9$ to 14	540	4.3	10
$Z = 15$ to 28	186	7.3	10
Secondary neutrons	4×10^4	0.5	10

6 Predicted Performance in the Martian Radiation Environment

We discuss here the required accumulated observation times necessary to obtain reasonable statistics for each of the various particle types. We begin by considering the most difficult case, the flux of GCR iron at or near solar maximum, when modulation is strongest and fluxes are relatively small. Using the Badhwar-O'Neill model for 2002, the total flux integrated over energy is about $6 \times 10^{-5} \text{ cm}^{-2} \text{ sr}^{-1} \text{ s}^{-1}$. Multiplying by RAD's $0.9 \text{ cm}^2 \text{ sr}$ geometry factor, 25 % duty cycle, and the 25 % probability that an iron ion survives traversal of the atmosphere without fragmentation, we obtain an overall average rate of 0.29 ions per day. Therefore, to obtain ± 10 % statistical accuracy will require ~ 345 days of accumulated observation time (about half of a Mars year). It can be seen in Fig. 20 that the flux of ions in the $Z = 3$ to 10 range is an order of magnitude higher than for the $Z = 21$ to 28 group (which is dominated by iron). Thus, integration times will be correspondingly shorter for other ion species, such as C and O. For example, even starting with the same low 2002 flux, we estimate RAD will detect about 7 carbon ions per day, so the ± 10 % statistical accuracy benchmark will be reached in two weeks of operations. Table 8 shows estimates for various particle types under these solar maximum conditions, with an atmospheric depth of 16 g cm^{-2} of CO_2 and with a 180-day accumulation at the nominal duty cycle. Also shown are required accuracy levels determined at the RAD Preliminary Design Review, based on evaluations of the present state of GCR, SEP, and transport model uncertainties. Given model uncertainties, measurements with these required accuracy levels were deemed sufficient to significantly improve our ability to test and validate existing models. It is these required accuracy levels that drove the instrument design, within the mass, volume and power constraints of the MSL mission.

Estimates were obtained starting with Badhwar-O'Neill GCR model fluxes. For helium and heavier ions, charge-changing cross sections from the NUCFRG2 code were used to estimate survival fractions through the atmosphere. Detector efficiencies for charged particles were assumed to be 100 %. The estimate of neutron counts was arrived at by integrating the lower neutron curve in Fig. 20 and multiplying by an assumed average efficiency of 1 %. It is worth noting that high-energy protons cannot be distinguished from high-energy pions or muons, and that there is no way to distinguish primary GCRs from secondaries. The total flux of charge-1 particles RAD will detect is therefore expected to be significantly higher than shown in Table 8. The helium flux will also be increased by secondaries produced in interactions of heavier ions, although those fluxes are relatively small. It is clear that RAD will meet the statistical requirements for all GCR measurements (and with large margins for all but the heaviest ions), even during solar maximum.

Table 9 shows the expected performance for RAD in the case of a large SEP event. For an average column depth of 16 g cm^{-2} CO_2 atmosphere, protons with energies below

Table 9 Expected statistics for large SEP events

Particle type	Number acquired per SEP event	Statistical accuracy (%)	Required accuracy (%)
Primary protons	7×10^5	0.1	5
Primary helium	1.4×10^3	2.6	10
Secondary neutrons	1.6×10^5	0.2	10

about 145 MeV will come to rest before reaching the surface. In typical SEP events, this will sharply limit the proton flux observed by RAD. De Angelis et al. (2007) modeled the large event of September 1989. They find that the fluxes of helium and neutrons at low energies are only slightly affected by assumptions about the regolith, and at energies above 1 MeV/nuc for helium and ~ 5 MeV for neutrons, their results are independent of the regolith model. The differential flux of protons at the surface peaks near 100 MeV, with levels approaching $10^5 \text{ cm}^{-2} \text{ MeV}^{-1}$, integrated over the event. Performing a rough integration of this flux above 150 MeV yields an event-integrated fluence on the order of 10^7 protons cm^{-2} on the Martian surface. Similar integration over the neutron fluence curve in the range 10 to 100 MeV yields an estimate of 10^7 neutrons cm^{-2} . The flux of helium in the 20 to 100 MeV/nuc range is estimated to be $\sim 2 \times 10^4$ ions cm^{-2} . These fluencies are divided by 4π and multiplied by the geometry factor to obtain the values in Table 9. For neutrons, a 1 % average detection efficiency is factored in.

We noted in Sect. 5.3.1 that RAD can detect ions with LET up to about 826 keV/ μm , corresponding to Fe at about 50 MeV/nuc. As can be seen in Fig. 20, even after passing through the Martian atmosphere, the vast majority of even the heaviest ions have higher energies than this. Thus, the dose contribution of particles with LET above RAD's saturation limit is accordingly expected to be very small. From the standpoint of dose equivalent, the quality factor at 800 keV/ μm is smaller by nearly a factor of 3 than at its peak, so again the contribution missed due to electronic saturation will be small.

Even with a 25 % duty cycle, RAD will meet its required statistical accuracy for even the heaviest GCR ions in less than 6 months on the Martian surface. Good statistics will be accumulated for lighter ions in a much shorter time. Calibration data show that RAD has the necessary wide dynamic range for charged particles, and has the capability to measure LET from 0.2 keV/ μm (minimum-ionizing charge-1 particles) to greater than 800 keV/ μm (slow heavy ions).

7 RAD Data Products

7.1 Data Flow

Events that match one or more L2 trigger masks are processed in L3, where a set of logical tests determines whether the event meets one of several pre-defined validity criteria. Valid events are counted, binned in the appropriate histogram, and in some cases pulse height analysis data (PHA records) are stored. At the end of an observing period, histogram and counter data are compressed and written, along with housekeeping and PHA records, to an “observation packet.” These 16384-byte packets contain all of RAD’s science data. Up to 1000 such packets can be stored in RAD’s non-volatile memory (NVRAM) at a given time, before being transferred to the RCE.

Table 10 EDR data products

Description	Identifier	Comments
RAE information	ERA	Includes VIRENA channel map, status of solar mode detection, etc.
System information	EDS	Detailed system status
Table checksums	ETX	EVIL, temperature, and setup tables
Messages	EMS	Array of messages up to 90 bytes
Number of EEPROM writes	EEW	Code and tables are stored in triplicate in EEPROM with limited number of lifetime write cycles
Built-in self-test (BIST)	EDB	Tests internal RAD memory
Housekeeping	EDH	Firmware status, EVIL and temperature table checksums, temperature and voltage readings
Normal-priority science data	ESD	One 16.4 kB packet/hour in nominal operations
High-priority science data	EHP	Produced during solar event mode and troubleshooting periods

On command from the RCE, RAD sends stored observation packets to the rover, where they are compressed and stored for relay to the ground. Once on the ground, the raw, compressed data is transferred to the MSL Operations Center (OC), where it is processed by the Operations Product Generation Subsystem (OPGS) to produce a set of Experiment Data Records (EDRs). All observation packets for a given sol are combined into a single EDR. Diagnostic and housekeeping EDR products are routinely created by the sequence that commands RAD to send its data to the RCE. These too are part of the per-sol set of EDR data products. EDR data products are then distributed by OPGS to the RAD project for further processing. The EDR products are input to the RAD Science Operations Center (SOC) data pipeline, which will produce Reduced Data Records (RDR). Descriptions of the RDR data products are being developed and will be made available in the RDR Software Interface Specification (SIS) for the Planetary Data System (PDS).

7.2 Overview of EDR Data Products

RAD EDR data products consist of the raw instrument data that is reformatted to conform to PDS standards. Detailed descriptions of these data are given in the RAD PDS Interface Control Document (ICD) and the EDR SIS document, available in the PDS archive. Higher-level products that include LET spectra, dose, etc., will be described in the RAD PDS ICD and the RDR SIS, also available in the PDS archive. These data will be made available as Quicklook data to the MSL team for tactical planning during surface operations. Although RAD data won't typically be used for tactical planning, RAD SEP event data may be used as a warning flag for other instruments in the event of a large SEP event.

RAD can send seven different types of data products to the RCE in response to various commands. On the ground, these data are turned into EDRs by OPGS. The EDR file types are listed in Table 10. Additional housekeeping data are included in the science data packets.

Each EDR data product has an associated three-character string as part of its (much longer) file name, which in all cases has the extension “DAT.” Each file type has an associated PDS “label” file that is also produced by OPGS, which gives a high-level description of the data product. More detailed descriptions of the contents of each file type are in the PDS “FMT” (format) files.

In the following sections, we give brief summaries of the different EDR data products generated by RAD, focusing mostly on the contents of the observation packets. We also provide an outline of the planned contents of the main RDR data products.

7.3 Diagnostic and Housekeeping EDRs

The diagnostic and housekeeping data products are meant for internal use and are not of interest to the vast majority of users. They are in the PDS archives for completeness, in large part owing to the nature of the data pipeline architecture for the MSL mission: the only RAD data that is available even to science team members comes through OPGS, and OPGS creates the full set of EDR data products. Users of RAD data in the science community will not need to use or interpret the diagnostic and housekeeping EDRs, since the science data products (described in the next section) and RDR's will be sufficiently detailed to enable analysis.

7.4 Science Data Products (Observation Data)

The binary observation packet files produced by OPGS are of two types, as shown in Table 10, regular priority (ESD) and high priority (EHP). There is no difference between the two file types except for the indication of priority in the file name. Observation packets are marked high priority if they are produced when RAD is in solar event mode (trigger rate above a pre-set threshold) or if they are created under certain specific troubleshooting circumstances. These two file types are, by definition, the EDR science data products. On the ground, they are altered from the observation packets created by RAD with the addition (by OPGS) of a 12-byte header and a 4-byte footer.

Each observation packet contains highly compressed science data acquired by RAD. The basic structure is shown in Table 11. Details of the histogram and PHA formats are not shown specifically here, but can be found in the EDR SIS supplied to the PDS.

7.4.1 *Science Data—Histograms*

As described previously, RAD does real-time analysis and histogramming of science data in L3. The L3 firmware receives data packets from L2, each packet consisting of a header and an event record. Contained within the event record are the fast tokens, slow tokens, and a variable number of ADC and (calibrated) ΔE values from the channels that were read out, as determined by the readout mask associated with the L2 trigger for the event. The event record also contains the weighted energy per detector determined by L2. Energy values are represented in units of 2 keV, which speeds processing.

Each particle type and energy leaves a specific pattern of energy deposited in the detectors, so that the combination of the ΔE measurements and the slow token mask can be used to identify the particle type and in some cases its energy. The L2 event data stream contains several hundred bytes per event, which must be compressed by a large factor. The most efficient way to do this is to create and fill histograms according to the type of particle that caused the event trigger. The function of the L3 analysis firmware is to take the event data, correctly interpret the deposited energy pattern, fill the appropriate histograms, and, in some cases, store a compressed PHA record.

Because RAD measures many types of particles over broad ranges of energy, many histograms are required to sort and store the data. The L3 firmware defines four categories of histograms: (1) dosimetry; (2) stopping charged particles; (3) penetrating charged particles;

Table 11 Observation packet structure

Field	Size (bytes)	Configurable	Description
CCSDS prime	6	N	CCSDS header with Spacecraft Clock (SCLK)
CCSDS SCLK	4	N	SCLK timestamp of packet
Block writes	2	N	Number of times this block has been written
Block	2	N	Bitfield: upper 4 bits= test mode, lower 12 bits = block number
Housekeeping	88	N	See EDR SIS for format details
System information		N	
Messages	100	N	
Science CCSDS	6	N	CCSDS for science produces (no SCLK)
Stopping A1 histogram	400	Y	See EDR SIS for format details
Stopping A2 histogram	400	Y	See EDR SIS for format details
Penetrating A2 histogram	160	Y	See EDR SIS for format details
Neutral D histogram	112	Y	See EDR SIS for format details
Neutral E histogram	112	Y	See EDR SIS for format details
Neutral D-E coincidence histogram	144	Y	See EDR SIS for format details
Counters	226	N	See EDR SIS for format details
Dosimetry histograms	314	Y	See EDR SIS for format details
Science packet checksum	4	N	Fletcher checksum for Science CCSDS packet
VIRENA	222	Y	CCSDS VIRENA settings
PHA CCSDS	6	Y	CCSDS wrapper for PHA data
PHA data	Varies	Y	8-bit compressed PHA records, fills whatever space remains in the 16.4 kB packet. See EDR SIS for format details
PHA checksum	4	Y	PHA CCSDS checksum
Detector select	5	N	Lowest 36 bits are a mask indicating which of the 36 hardware channels have been selected (maximum of 32)
Observation packet checksum	4	N	Last 4 bytes of the packet (bytes 16381-4)
Extra PHA	Varies	Y	Optional extra 16 kB packet of PHA data
Level 2 configuration		Y	Dump of Level 2 configuration used

and (4) neutral particles. Within each category there are multiple histograms, some of which are one-dimensional, others two-dimensional. Table 12 lists these histograms. In all cases, “log” refers to the RDE_log2 approximation described in Sect. 3.2.2. The abbreviation “T” is used for total energy, i.e., the sum of ΔE ’s in A, B, C, D, and E. Although E is often used for energy, here when we mean energy deposited we use ΔE , and we use E to mean ΔE in the E detector.

To be entered into the histograms, events must satisfy a number of defined selection criteria (cuts). For events with low hardware priority (low-LET), the cuts depend on slow token values. For events with high hardware priority (high-LET), higher fidelity is required, so different cut logic is used based on ΔE readings. Numerical cut values are loaded into RAD as firmware parameters. The selection logic is hard-coded for both priority cases, but

Table 12 List of L3 histograms

Histogram group	# of histograms in group	Description	Quantity plotted or summed	Comments
Dosimetry: B dose (1-d)	4	Dose in B detector	ΔE in B summed	16 time bins, 16 ΔE bins, 2 priorities
Dosimetry: LET in B (1-d)	4	LET in B	$\log(\Delta E$ in B)	A1 or A2 hit, 2 priorities
Dosimetry: E dose (1-d)	4	Dose in E detector	ΔE in E	16 time bins, 16 ΔE bins, 2 priorities
Stopping charged particles (2-d)	4	Charged particles that stop in C, D, or E	$x = \log(T/A)$ $y = \log(T \cdot A)$	A1 or A2 hit, 2 priorities
Penetrating charged particles (2-d)	2	Charged particles hitting A2 and B, C, D, E and F	$x = \log(A + B + C)$ $y = \log[E/(A + B + C)]$	A2 hit, 2 priorities
Neutral particles (2-d)	2	Neutral particles that deposit energy in D and/or E	$x = \log(D)$ $y = \log(E)$	2 priorities
Neutral (1-d)	4	Neutral particles in D, E are treated separately	$\log(D)$ $\log(E)$	2 priorities each

the cut values for high-priority events are configurable. The performance of the L3 firmware thus depends on the loading of appropriate cut values.

The conceptual basis of the stopping and penetrating charged-particle histograms is illustrated in Fig. 22, using a simulation of GCR fluxes transported through the Martian atmosphere. For plotting purposes, the proton flux has been arbitrarily scaled down by a factor of 8. The upper plot approximates the onboard two-dimensional histogram for penetrating particles. Only protons and helium are shown. Three clusters are visible: protons, most densely populating the area around (7, 4); well-measured helium ions, most densely populating around (8.8, 4); and helium ions that undergo fragmentation in the D detector (8.8, 2). The upward-turning tails are due to slower ions that lose significant energy in traversing D, so that by the time they reach E, their dE/dx has increased substantially compared to what it was in traversing A, B, and C. Protons and helium are well-separated and the y value can be related to the incident energy.

The lower plot in Fig. 22 contains an approximation of the stopping-particle histogram, with all ions shown. At relatively low energies, one can approximate dE/dx as being proportional to Z^2/E_{tot} . The y-axis in this plot then goes approximately as the logarithm of $(E_{\text{tot}} \times dE/dx \sim Z^2)$, while the x-axis goes approximately as the logarithm of $(E_{\text{tot}}/dE/dx \sim (E_{\text{tot}})^2)$. Thus this plot is, in essence, charge vs. energy. The two well-populated, nearly-horizontal bands are due to protons (lower) and helium (upper), which again are well-separated. Much fainter bands can be seen for heavier ions. Note that in both plots in Fig. 22, the color scale indicates the number of events, with logarithmic sensitivity.

A PHA storage priority, in the range 0 to 3, is assigned to a charged particle event depending upon which bin of the two-dimensional histogram it falls in. PHA priorities increase moving to the right and upward. The bottom- and left-most regions of the histograms will

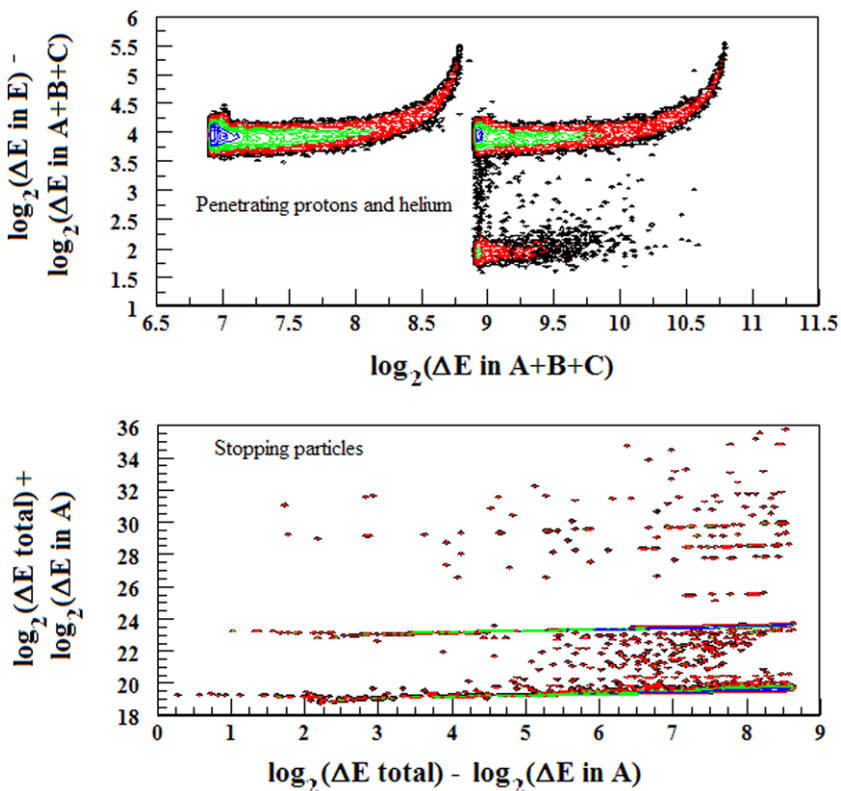


Fig. 22 Facsimiles of the onboard histograms for penetrating charged particles (*upper*) and stopping charged particles (*lower*). Data from a model calculation are shown; GCR fluxes from the Badhwar-O’Neill model for the 2002 solar maximum were transported through 16 g cm^{-2} of CO_2 and then through RAD

be populated by protons and helium, for which a small fraction of PHA records can be kept before the buffer fills up. In contrast, heavy ions and relatively slow particles will (sparsely) populate the regions further to the right and higher in the histograms, so PHA records for virtually all of these events will be kept. This will allow for much more detailed analysis on the ground.

7.4.2 Science Data—Counters

The counter data stored by RAD give valuable information about the radiation environment and RAD’s performance. The counter data stored in the observation packet is summarized in Table 13.

As described in Sect. 3, each of the 32 VIRENA channels has an associated fast and slow token. For each of these, a counter is kept. These are referred to as the Level 1, or L1, counters. There are also two counters for each of the sixteen L2 triggers: one that counts the number of times the slow token pattern matched the definition of that trigger, and another that counts the number of times such events are actually read out. (Readout will not occur if the FIFO for transmission from the EVIL to the RDE is full, or if the event is low priority and the FIFO is more than half full.) The L2 matching firmware assigns a hardware priority to each event (see Table 5), and counters are kept for the number of times each priority is

Table 13 Counter data description

Field	Size (bytes)	Compressed	Description
Sync	2	n	0xEDE9
Apid	2	n	0x701
Length	2	n	Length of packet, in bytes
Fast_token(32)	64	y	Fast token counts
Slow_token(32)	64	y	Slow token counts
L2Trig_counters(16)	32	y	L2 trigger counts
L2Trig_reads(16)	32	y	L2 trigger readouts
Lo_pri_cnt	2	y	Count of low-priority L2 triggers
Hi_pri_cnt	2	y	Count of high-priority L2 triggers
Lo_pri_readout	2	y	Low-priority L2 triggers read out
Hi_pri_out	2	y	High-priority L2 triggers read out
Fast_trig_cnt	2	y	Fast trigger counts, all channels
Dead_time_cnt	2	y	Dead time count (number of 10.67 μ s clock ticks when front-end is disabled)
Alive_time_cnt	2	y	Alive time count (number of 10.67 μ s clock ticks when front-end is enabled)
Reserved	2	y	Reserved
PHA_pri_3	2	y	PHA storage priority 3 counts (highest)
PHA_pri_2	2	y	PHA storage priority 2 counts
PHA_pri_1	2	y	PHA storage priority 1 counts
PHA_pri_0	2	y	PHA storage priority 0 counts (lowest)
Checksum	4	n	Fletcher checksum

assigned, as well as for the number of times events with that priority are read out. The alive and dead time counts refer to Level 1, which at any given time may be available (alive) or busy processing an event (dead). We define the quantity L to be the ratio of alive time to the sum of dead and alive times, and is one ingredient of the livetime corrections needed to normalize the data. The priority counts (rows 8 and 9 of Table 13) and their associated priority readout counts (rows 10 and 11) are also needed. As should be evident, the two different event priorities will in general require different correction factors to account for the separate handling of events in the FIFO (see Sect. 3.2.1). This gives rise to two factors, f_0 and f_1 , defined respectively as $f_i = (\text{readouts of priority } i)/(\text{counts of priority } i)$.

An additional correction must be applied to PHA data. For each PHA storage priority, some fraction of events will be stored (e.g. typically 100 % of Priority 3 events will be stored). If the stored fraction of any buffer is less than 1, and absolute normalization of a spectrum derived from PHA data is needed, then a correction factor is needed.

Consider the following example to help clarify the discussion. For instance, in producing the RDR's, it will be necessary to combine pairs of identically-binned histograms. In each pair, one histogram is populated by low-priority events, the other by high-priority events. We take the case of two-dimensional histograms, with a number of counts N_{ij} in some arbitrary

bin labeled i for the x -axis and j for the y -axis. The corrected number of counts in bin (i, j) of the summed histogram is then given by:

$$N_{ij}^{\text{corr}} = \frac{N_{ij}^{\text{low}} f_0 + N_{ij}^{\text{high}} f_1}{L}$$

The correction factors are slightly more complicated than this (but similar in principle) for normalizing spectra based on PHA data.

7.4.3 Science Data—PHA Event Records

From Table 10, one can see that ~ 14 kB of the observation packet is available for PHA records. In a typical observation packet, we expect that roughly 300 such records will be stored. The exact number depends on the record sizes, which are determined by the L2 readout mask. For example, only about half of the available channels are read out on neutral particle events, so those records are relatively small. In contrast, for a high-LET charged particle event, all 32 channels are read out, producing a larger record. The number of stored PHA records will therefore likely be different for any given observation packet.

In a 16-minute observation, assuming a charged-particle flux of $\sim 5 \text{ cm}^{-2} \text{ sr}^{-1} \text{ s}^{-1}$, RAD will measure about 4300 events, and likely a comparable number of neutral-particle events. (Trigger threshold settings for D and E will determine those rates, and will not be finalized until some time after landing.) Only a small fraction, on the order of 5 % of the total, can be stored. But the priority scheme guarantees that PHA records for the events of the greatest interest, which are expected to comprise on the order of 1 % of the total, will be stored.

PHA records within the observation packet are delimited by a sync byte (hexadecimal ‘BEEF’). The first byte after this contains a hardware priority bit, two PHA priority bits, and the four-bit (1/16th resolution) time tag within the observation period. This is followed by the 4-byte slow token mask, the 4-byte readout mask, the two-byte L2 trigger mask, and then a series of 1-byte ADC values, one for each channel in the readout mask. An event with a full 32-channel readout therefore has a 43-byte PHA record.

The ADC digitizes pulse heights in 14 bits, so the maximum value is 16383. In L2 processing, the pedestal (typically ~ 1500 ADC counts) is subtracted, and then a small offset is added back in so that the entire width of the noise peak for each channel is represented in the PHA records. These PHA values are then compressed into a one-byte format in which the top 3 bits are the exponent and the lower 5 bits the mantissa with an implicit leading 1.

7.5 RDR Data Products

The RDR data products will be human-readable and will contain higher-level science information than is available in the EDR. Creation of the RDR data products from the EDR’s will be accomplished via a Structured Query Language (SQL) database running on the RAD SOC server. The database ingests all EDR products received from OPGS.

Some fields in the EDR (housekeeping, messages, etc.) will simply be translated from binary to ASCII. Counter data will be un-compressed and output in time series and per-sol totals. The onboard histograms will be combined and properly normalized (see Sect. 7.4.1), and put into more conventional physical units (e.g. MeV instead of 2 keV) where appropriate. Details of the RDR data product formats will be available in the RDR SIS stored with the PDS.

7.6 Data Archive and Distribution

The RAD team has a data policy consistent with the MSL “Rules of the Road.” A subset of RAD data products will be made available to the science community and public as quickly as automated data transfer, quality control, and web posting allows. Once the EDR data from MSL arrives at RAD SOC, it will usually be available to the MSL team in less than one hour. EDR and higher-level data products are submitted and archived to PDS typically within several weeks of RAD SOC acquisition. A public web interface to the data will also permit retrieval of all data products generated by the RAD-SOC computer, after the data have been released to the PDS.

PDS archives of EDR data will be produced by JPL’s OPGS, and PDS archives of RDR data products will be created by the RAD SOC. These will be archived to the PDS, nominally in 90 sol (day) bundles every three months after the first delivery is released by the PDS to the public (nominally 3–6 months after landing).

Acknowledgements RAD is supported by NASA (HEOMD) under JPL subcontract #1273039 to Southwest Research Institute and in Germany by DLR and DLR’s Space Administration grant 50QM0501 to the Christian-Albrechts-University (CAU) Kiel. We would like to extend a huge thanks to Jeff Simmonds (MSL Payload Manager) and the Project Science Team John Grotzinger, Joy Crisp, and Ashwin Vasavada, the NASA Program Scientist Michael Meyer, and the first Project Scientist Edward Stolper. We would also like to extend a special thanks to Chris Moore and Gale Allen at NASA HQ (HEOMD) and Heiner Witte at DLR in Germany for their unwavering support of RAD over the years. Support for RAD calibration beam time at BNL/NSRL has been provided by the NASA HRP Program. We also thank the management and operators of the HIMAC facility at NIRS (Chiba, Japan), TSL in Uppsala, Sweden, and iThemba Labs in South Africa for their many hours of excellent beam time and support of RAD calibration.

References

- S. Agostinelli et al., GEANT4—a simulation toolkit. *Nucl. Instrum. Methods A* **506**, 250 (2003)
- G. Battistoni et al., Hadronic models for cosmic ray physics: the FLUKA code. *Nucl. Phys. B* **175–176**, 88 (2008)
- G.A. Bazilevskaya et al., Cosmic ray induced ion production in the atmosphere. *Space Sci. Rev.* **137**, 149 (2008)
- J.-P. Bibring et al., Global mineralogical and aqueous Mars history derived from OMEGA/Mars Express data. *Science* **312**(5772), 400 (2006)
- J.B. Birks, *The Theory and Practice of Scintillation Counting* (Pergamon Press, New York, 1964)
- D. Blake, D. Vaniman, R. Anderson, D. Bish, S. Chipera, S. Chemtob, J. Crisp et al., The CheMin mineralogical instrument on the Mars Science Laboratory mission, in *40th Lunar and Planetary Science Conference*, March 23–27, 2009, Paper #1484
- W.V. Boynton et al., Distribution of hydrogen in the near surface of Mars: Evidence for subsurface ice deposits. *Science* **297**, 81 (2002)
- W.V. Boynton et al., The Mars Odyssey Gamma-Ray Spectrometer instrument suite. *Space Sci. Rev.* **110**, 37 (2004)
- M.A. Bullock, J.M. Moore, Atmospheric conditions on early Mars and the missing layered carbonates. *Geophys. Res. Lett.* **34**, L19201 (2007)
- M.A. Bullock, C.R. Stoker, C.P. McKay, A.P. Zent, A coupled soil-atmosphere model of H_2O_2 on Mars. *Icarus* **107**, 142 (1994)
- W.R. Burrus, V.V. Verbinski, Fast-neutron spectroscopy with thick organic scintillators. *Nucl. Instrum. Methods* **67**, 181 (1969)
- H.V. Cane, L.G. Richardson, T.T. von Rosenvinge, A study of solar energetic particle events of 1997–2006: Their composition and associations. *J. Geophys. Res.* **115**, A08101 (2010)
- C.R. Chapman, Space weathering of asteroid surfaces. *Annu. Rev. Earth Planet. Sci.* **32**, 539–567 (2004)
- P. Chowdhury, B.N. Dwivedi, P.C. Ray, Solar modulation of galactic cosmic rays during 19–23 solar cycles. *New Astron.* **16**, 430 (2011)
- P.R. Christensen, Formation of recent Martian gullies through melting of extensive water-rich snow deposits. *Nature* **422**, 45 (2003)

- M.S. Clowdsley, J.W. Wilson, M.-Y. Kim, R.C. Singleterry, R.K. Tripathi, J.H. Heinbockel, F.F. Badavi, J.L. Shinn, Neutron environments on the Martian surface. *Phys. Med.* **17**(Suppl. 1), 94 (2001)
- R. Craun, D. Smith, Analysis of response data for several organic scintillators. *Nucl. Instrum. Methods* **80**, 239–244 (1970)
- F.A. Cucinotta, L.J. Chappell, Updates to radiation risks limits for astronauts: risks for never-smokers. *Radiat. Res.* **176**, 102 (2011)
- F.A. Cucinotta, W. Schimmerling, J.W. Wilson, L.E. Peterson, G.D. Badhwar, P.B. Saganti, J.F. Dicello, Space radiation cancer risks and uncertainties for Mars missions. *Radiat. Res.* **156**, 682 (2001)
- F.A. Cucinotta, P.B. Saganti, J.W. Wilson, L.C. Simonsen, Model predictions and visualization of the particle flux on the surface of Mars. *J. Radiat. Res.* **43**, S35 (2002)
- F.A. Cucinotta, M. Durante, Cancer risk from exposure to galactic cosmic rays: implications for space exploration by human beings. *Lancet Oncol.* **7**, 431 (2006)
- F.A. Cucinotta, M.-Y. Kim, S.I. Schneider, D.M. Hassler, Description of light ion production cross sections and fluxes on the Mars surface using the QMSFRG model. *Radiat. Environ. Biophys.* **46**, 101 (2007)
- F.A. Cucinotta, L. Chappell, M.Y. Kim, Space radiation cancer risk projections and uncertainties—2010, NASA TP 2011-216155 (2011)
- L.R. Dartnell, L. Desorgher, J.M. Ward, A.J. Coates, Modelling the surface and subsurface Martian radiation environment: implications for astrobiology. *Geophys. Res. Lett.* **34**, L02207 (2007a)
- L.R. Dartnell, L. Desorgher, J.M. Ward, A.J. Coates, Martian sub-surface ionizing radiation: biosignatures and geology. *Biogeosciences* **4**, 545–558 (2007b)
- G. De Angelis, J.W. Wilson, M.S. Clowdsley, G.D. Qualls, R.C. Singleterry, Modeling of the Martian environment for radiation analysis. *Radiat. Meas.* **41**, 1097 (2006)
- G. De Angelis, F.F. Badavi, S.R. Blattning, M.S. Clowdsley, J.E. Nealy, G.D. Qualls, R.C. Singleterry, R.K. Tripathi, J.W. Wilson, Modeling of the Martian environment for radiation analysis. *Nucl. Phys. B* **166**, 184 (2007)
- G.T. Delory, J.G. Luhmann, D. Brain, R.J. Lillis, D.L. Mitchell, R.A. Mewaldt, T.V. Falkenberg, Energetic particles detected by the Electron Reflectometer instrument on the Mars Global Surveyor, 1999–2006. *Space Weather* (2012). doi:[10.1029/2012SW000781](https://doi.org/10.1029/2012SW000781)
- L. Dorman, L. Pustil'nik, A. Sternlieb, I. Zukerman, Using ground-level cosmic ray observations for automatically generating predictions of hazardous energetic particle levels. *Adv. Space Res.* **31**, 847 (2003)
- B.G. Drake (ed.), *Human Exploration of Mars Design Reference Architecture 5.0*. NASA/SP-2009-566 (2009)
- B. Ehresmann, S. Burmeister, R.-F. Wimmer-Schweingruber, G. Reitz, Influence of higher atmospheric pressure on the Martian radiation environment: Implications for possible habitability in the Noachian epoch. *J. Geophys. Res.* **116**, A10106 (2011)
- G. Failla, Biological effects of ionizing radiations. *J. Appl. Phys.* **12**, 279 (1941)
- A.G. Fairén, D. Schulze-Makuch, A.P. Rodríguez, W. Fink, A.F. Davila, E.R. Uceda, R. Furfarro, R. Amils, C.P. McKay, Evidence for Amazonian acidic liquid water on Mars—A reinterpretation of MER mission results. *Planet. Space Sci.* **57**, 276 (2009)
- A. Fassò et al., The FLUKA code: present application and future developments, in *Computing in High Energy and Nuclear Physics*, La Jolla, CA, USA (2003)
- F. Forget, R.T. Pierrehumbert, Warming early Mars with carbon dioxide clouds that scatter infrared radiation. *Science* **278**, 1273 (1997)
- J. Gómez-Elvira et al. (REMS team), Environmental monitoring station for Mars Science Laboratory, in *Third International Workshop on the Mars Atmosphere: Modeling and Observations*, Williamsburg, Virginia, November 10–13, 2008
- D. Grinspoon, *Lonely Planets: The Natural Philosophy of Alien Life* (HarperCollins, New York, 2003)
- R.M. Haberle, Early Mars climate models. *J. Geophys. Res.* **103**(28), 28,467–28,479 (1998)
- R.M. Haberle, J.B. Pollack, J.R. Barnes, R.W. Zurek, C.B. Leovy, J.R. Murphy, J. Schaeffer, H. Lee, Mars atmospheric dynamics as simulated by the NASA/Ames general circulation model I. The zonal mean circulation. *J. Geophys. Res.* **98**, 3093 (1993)
- R.M. Haberle et al., Orbital change experiments with a Mars General Circulation Model. *Icarus* **161**, 66–89 (2003)
- B. Hapke, Space weathering from Mercury to the asteroid belt. *J. Geophys. Res.* **106**, 10,039 (2001)
- D.H. Hathaway, A standard law for the equatorward drift of the sunspot zones. *Sol. Phys.* **273**, 221 (2011)
- J.W. Head, L. Wilson, K.L. Mitchell, Generation of recent massive water floods at Cerberus Fossae, Mars by dike emplacement, cryospheric cracking, and confined aquifer groundwater release. *Geophys. Res. Lett.* **30**, 1577 (2003)
- M. Hecht et al., Detection of perchlorate and the soluble chemistry of the Martian soil at the Phoenix lander site. *Science* **325**, 64–67 (2009)

- S.L. Hess, R.M. Henry, C.B. Leovy, J.A. Ryan, J.E. Tillman, Meteorological results from the surface of Mars: Viking 1 and 2. *J. Geophys. Res.* **82**, 4559 (1977)
- S.L. Hess, R.M. Henry, J.E. Tillman, The seasonal variation of atmospheric pressure on Mars as affected by the south polar cap. *J. Geophys. Res.* **84**, 2923 (1979)
- International Commission on Radiological Protection (ICRP), ICRP Publication 60: 1990 Recommendations of the International Commission on Radiological Protection, *Ann. ICRP* **21** (1–3) (1991)
- B.M. Jakosky, R.C. Reedy, J. Masarik, Carbon 14 measurements of the Martian atmosphere as an indicator of atmosphere-regolith exchange of CO₂. *J. Geophys. Res.* **101**, 2247 (1996)
- J.R. Johnson, W.M. Grundy, M.T. Lemmon, Dust deposition at the Mars Pathfinder landing site: observations and modeling of visible/near-infrared spectra. *Icarus* **163**, 330 (2003)
- J. Köhler, B. Ehresmann, C. Martin, E. Böhm, A. Kharytonov, O. Kortmann, C. Zeitlin, D.M. Hassler, R.F. Wimmer-Schweingruber, Inversion of neutron/gamma spectra from scintillator measurements. *Nucl. Instrum. Methods B* **269**, 2641 (2011)
- O. Kortmann, Scintillator performance investigation for MSL/RAD, Ph.D. thesis, Christian-Albrechts-Universität zu Kiel (2010)
- J. Laskar, B. Levrard, J.F. Mustard, Orbital forcing of the Martian polar layered deposits. *Nature* **419**, 375–377 (2002)
- J.G. Luhmann, C. Zeitlin, R. Turner, D.A. Brain, G. Delory, L.G. Lyon, W. Boynton, Solar energetic particles in near-Mars space. *J. Geophys. Res.* **112**, E10001 (2007)
- P.R. Mahaffy et al., The sample analysis at Mars investigation and instrument suite. *Space Sci. Rev.* (2012). doi:[10.1007/s11214-012-9879-z](https://doi.org/10.1007/s11214-012-9879-z)
- F.B. McDonald, G.H. Ludwig, Measurement of low energy primary cosmic ray protons on the IMP-1 satellite. *Phys. Rev. Lett.* **13**, 783 (1964).
- R.A. Mewaldt et al., Galactic Cosmic Ray intensities reach record levels in 2009, in *American Geophysical Union Fall Meeting*, 2009, abstract #SH13C-08
- C. Mileikowsky, F. Cucinotta, J.W. Wilson, B. Gladman, G. Horneck, L. Lindgren, H.J. Melosh, H. Rickman, M.J. Valtonen, J.Q. Zheng, Natural transfer of viable microbes in space. Part 1: From Mars to Earth and Earth to Mars. *Icarus* **145**, 391–427 (2000)
- I. Mitrofanov et al., Maps of subsurface hydrogen from the High Energy Neutron Detector, Mars Odyssey. *Science* **297**, 78 (2002)
- R. Müller-Mellin et al., COSTEP—comprehensive suprathermal ad energetic particle analyzer. *Sol. Phys.* **162**, 483 (1995)
- K. Nakamura et al. (Particle Data Group), Review of particle physics. *J. Phys. G, Nucl. Part. Phys.* **37**, 075021 (2010)
- NCRP (National Council on Radiation Protection & Measurements), Report No. 132—Radiation Protection Guidance for Activities in Low-Earth Orbit (2000)
- NRC (National Research Council), Committee on the Evaluation of Radiation Shielding for Space Exploration, *Managing Space Radiation Risk in the New Era of Space Exploration* (National Academies Press, Washington, 2008). Chap. 3: “Radiation Effects” and references therein
- P.M. O’Neill, Badhwar-O’Neill 2010 galactic cosmic ray flux model—revised. *IEEE Trans. Nucl. Sci.* **57**, 3148 (2010)
- N. Pace, The universal nature of biochemistry. *Proc. Natl. Acad. Sci. USA* **98**, 805 (2001)
- A.K. Pavlov, A.V. Blinov, A.N. Konstantinov, Sterilization of Martian surface by cosmic radiation. *Planet. Space Sci.* **50**, 669 (2002)
- G. Pfotzer, Dreifachkoinzidenzen der Ultrastrahlung aus vertikaler Richtung in der Stratosphäre. *Z. Phys.* **102**, 23 (1936)
- J.B. Pollack, J.F. Kasting, S.M. Richardson, K. Poliakoff, The case for a wet, warm climate on early Mars. *Icarus* **71**, 203 (1987)
- A. Posner, H. Kunow, Energy dispersion in solar ion events over 4 orders of magnitude: SOHO/COSTEP and Wind/STICS, in *Proc. 28th Intern. Cosmic Ray Conf.*, Tsukuba, ed. by T. Kajita et al., vol. 6 (Univ. Acad. Press, Tokyo, 2003), p. 3309
- A. Posner, D.M. Hassler, D.J. McComas, S. Rafkin, R.F. Wimmer-Schweingruber, E. Bohm, S. Bottcher, S. Burmeister, W. Droege, B. Heber, A high energy telescope for the Solar Orbiter. *Adv. Space Res.* **36**, 1426 (1995)
- A.V. Prokofiev, O. Byström, C. Ekström, V. Ziemann, J. Blomgren, S. Pomp, M. Österlund, U. Tippawan, A new neutron beam facility at TSL, in *International Workshop on Fast Neutron Detectors*, University of Cape Town, South Africa, April 3–6, 2006
- R.C. Reedy, S.D. Howe, The Martian radiation environment from orbit and on the surface, in *Workshop on Mars 2001: Integrated Science in Preparation for Sample Return and Human Exploration*, Lunar and Planetary Institute, Houston, TX, Oct 2–4, 1999

- P.B. Saganti, F.A. Cucinotta, J.W. Wilson, L.C. Simonsen, C. Zeitlin, Radiation climate map for analyzing risks to astronauts on the Mars surface from galactic cosmic rays. *Space Sci. Rev.* **110**, 143 (2004)
- J.T. Schofield, J.R. Barnes, D. Crisp, R.M. Haberle, S. Larsen, J.A. Magalhães, J.R. Murphy, A. Seiff, G. Wilson, The Mars Pathfinder Atmospheric Structure Investigation & Meteorology (ASI/MET) Experiment. *Science* **278**, 1752 (1997)
- N.A. Schwadron et al., Lunar radiation environment and space weathering from the Cosmic Ray Telescope for the Effects of Radiation (CRaTER). *J. Geophys. Res.* **117**, E00H13 (2012)
- A.L. Sprague, W.V. Boynton, K.E. Kerry, D.M. Janes, D.M. Hunten, K.J. Kim, R.C. Reedy, A.E. Metzger, 'Mars' south polar Ar enhancement: A tracer for south polar seasonal meridional mixing. *Science* **306**, 1364 (2004)
- A.L. Sprague, W.V. Boynton, K.E. Kerry, D.M. Janes, N.J. Kelly, M.K. Crombie, S.M. Nelli, J.R. Murphy, R.C. Reedy, A.E. Metzger, Mars' atmospheric argon: Tracer for understanding Martian atmospheric circulation and dynamics. *J. Geophys. Res.* **112**, E03S02 (2007)
- S.W. Squyres, A.H. Knoll, Sedimentary rocks at Meridiani Planum: Origin, diagenesis, and implications for life on Mars. *Earth Planet. Sci. Lett.* **240**, 1 (2005)
- J.E. Tillman, Mars global atmospheric oscillations: Annually synchronized, transient normal-mode oscillations and the triggering of global dust storms. *J. Geophys. Res.* **93**, 9433 (1988)
- L.W. Townsend, J.E. Nealy, J.W. Wilson, L.C. Simonsen, Estimates of galactic cosmic ray shielding requirements during solar minimum, NASA TM-4167 (1990)
- L.W. Townsend, J.L. Shinn, J.W. Wilson, Interplanetary crew exposure estimates for the August 1972 and October 1989 Solar Particle Events. *Radiat. Res.* **126**, 108–110 (1991)
- V.I. Tretyakov, A.S. Kozyrev, M.L. Litvak, A.V. Malakhov, I.G. Mitrofanov, M.I. Mokrousov, A.B. Sanin, A.A. Vostrukhin, Comparison of neutron environment and neutron component of radiation dose for space around Earth and Mars from data of instruments HEND/Mars Odyssey and BTN/ISS, in *40th Lunar and Planetary Science Conference* (2009), paper #1292
- R.K. Tripathi, J.E. Nealy, Mars radiation risk assessment and shielding design for long-term exposure to ionizing space radiation, in *IEEE Aerospace Conference*, March 1–8, 2008, paper #1291
- L.S. Waters, G.W. McKinney, J.W. Durkee, M.L. Fensin, J.S. Hendricks, M.R. James, R.C. Johns, D.B. Pelowitz, The MCNPX Monte Carlo radiation transport code. *AIP Conf. Proc.* **896**, 81 (2007)
- J.W. Wilson, J.L. Shinn, L.W. Townsend, R.K. Tripathi, F.F. Badavi, S.Y. Chun, NUCFRG2: a semiempirical nuclear fragmentation model. *Nucl. Instrum. Methods B* **94**, 95–102 (1994)
- J.W. Wilson, F. Badavi, F.A. Cucinotta, J.L. Shinn, G.D. Badhwar, R. Silberberg, C.H. Tsao, L.W. Townsend, R.K. Tripathi et al. HZETRN: Description of a free-space ion and nucleon transport and shielding computer program, NASA Technical Paper No. 3495 (1995)
- J.W. Wilson, M.Y. Kim, M.S. Clowdsley, J.H. Heinbockel, R.K. Tripathi, R.C. Singletary, J.L. Shinn, R. Suggs, Mars surface ionizing radiation environment: Need for validation, in *Workshop on Mars 2001: Integrated Science in Preparation for Sample Return and Human Exploration, Lunar and Planetary Institute*, Houston, TX, Oct 2–4, 1999
- J.W. Wilson, F.A. Cucinotta, M.-H.Y. Kim, W. Schimmerling, Optimized shielding for space radiation protection. *Phys. Med. XVII*(Suppl. 1), 67 (2001)
- C.H. Yang, L.M. Craise, M. Durante, M. Mei, Heavy-ion induced genetic changes and evolution processes. *Adv. Space Res.* **14**, 373 (1994)
- C. Zeitlin, L. Heilbronn, J. Miller, W. Schimmerling, L.W. Townsend, R.K. Tripathi, J.W. Wilson, The fragmentation of 510 MeV/nucleon Iron-56 in polyethylene, II. Comparisons between data and a model. *Radiat. Res.* **145**, 666 (1996)
- C. Zeitlin, D.M. Hassler et al., Mars Odyssey measurements of galactic cosmic rays and solar particles in Mars orbit, 2002–2008. *Space Weather* **8**, S00E06 (2010a)
- C. Zeitlin, S. Guetersloh, L. Heilbronn, J. Miller, A. Fukumura, Y. Iwata, T. Murakami, L. Sihver, Nuclear fragmentation database for GCR transport code development. *Adv. Space Res.* **46**, 728 (2010b)
- A.P. Zent, C.P. McKay, The chemical reactivity of the Martian soil and implications for future missions. *Icarus* **108**, 146–157 (1994)
- A.P. Zent, R.C. Quinn, Simultaneous adsorption of CO₂ and H₂O under Mars-like conditions and application to the evolution of the Martian climate. *J. Geophys. Res.* **100**, 5341 (1995)